nature communications

Article

https://doi.org/10.1038/s41467-025-56024-4

Trajectory analysis of hepatic stellate cell differentiation reveals metabolic regulation of cell commitment and fibrosis

Received: 5 January 2024

Accepted: 7 January 2025

Published online: 10 February 2025

Check for updates

Raquel A. Martínez García de la Torre[1,2], Julia Vallverdú[1], Zhenqing Xu[1,2], Silvia Ariño[1,2,3], Raquel Ferrer-Lorente[1], Laura Zanatto[1,2], Maria Mercado-Gómez[1], Beatriz Aguilar-Bravo[1], Paloma Ruiz-Blázquez[1,2,3,4], Maria Fernandez- Fernandez[1,2,3,4], Artur Navarro-Gascon[5,6], Albert Blasco-Roset[5,6], Paula Sànchez-Fernàndez-de-Landa[5,7], Joan Pera[8], Damia Romero-Moya[8], Paula Ayuso Garcia[9], Celia Martínez Sánchez[1,2,3], Laura Sererols Viñas[1,2], Paula Cantallops Vilà[1,2], Carmen I. Cárcamo Giráldez[1], Andrew McQuillin[10], Marsha Y. Morgan[11], Daniel Moya-Rull[12], Núria Montserrat[12,13], Delphine Eberlé[14], Bart Staels[14], Bénédicte Antoine[15], Mikel Azkargorta[3,16], Juan-José Lozano[3], Maria L. Martínez-Chantar[3,17], Alessandra Giorgetti[8,18], Félix Elortza[3,16], Anna Planavila[5,6], Marta Varela-Rey[9,18], Ashwin Woodhoo[9,19,20], Antonio Zorzano[5,6,7,21], Isabel Graupera[1,3,22], Anna Moles[1,3,4], Mar Coll[1,2,23], Silvia Affo[1] ✉ & Pau Sancho-Bru[1,3,23] ✉

Defining the trajectory of cells during differentiation and disease is key for uncovering the mechanisms driving cell fate and identity. However, trajectories of human cells remain largely unexplored due to the challenges of studying them with human samples. In this study, we investigate the proteome trajectory of iPSCs differentiation to hepatic stellate cells (diHSCs) and identify RORA as a key transcription factor governing the metabolic reprogramming of HSCs necessary for diHSCs' commitment, identity, and activation. Using RORA deficient iPSCs and pharmacologic interventions, we show that RORA is required for early differentiation and prevents diHSCs activation by reducing the high energetic state of the cells. While RORA knockout mice have enhanced fibrosis, RORA agonists rescue multi-organ fibrosis in in vivo models. Notably, RORA expression correlates negatively with liver fibrosis and HSCs activation markers in patients with liver disease. This study reveals that RORA regulates cell metabolic plasticity, important for mesoderm differentiation, pericyte quiescence, and fibrosis, influencing cell commitment and disease.

During embryonic development cells undergo a transcriptomic and metabolic reprogramming controlled by pathways tightly regulated in a time, space, and cell-dependent manner. When the embryonic development ends, homeostasis takes over. Nonetheless, developmental signaling pathways can be reactivated for the maintenance and repair of adult tissues[1]. Therefore, it is fundamental to investigate the mechanisms governing cell identity and their fate upon development and disease to better define the differentiation paths and

A full list of affiliations appears at the end of the paper. ✉e-mail: saffo@recerca.clinic.cat; psancho@recerca.clinic.cat

understand cell trajectories in space and time. In this context, human induced pluripotent stem cells (iPSCs) are a promising and useful tool, as they can differentiate into any cell type, and can be shaped in vitro to mimic a disease condition, offering the possibility to study cell physiological and pathophysiological trajectory[2,3].

Fibrosis is an evolutionary conserved mechanism involved in multiple chronic injury conditions and tissues and is responsible for nearly 45% of all death in industrialized countries, being the liver one of the principal organs affected[4]. Liver fibrosis is the common outbreak of most liver diseases and is associated with the risk of mortality and liver-related morbidity[5]. The main cell type responsible for liver fibrosis are hepatic stellate cells (HSCs)[6]. These cells are specialized liver pericytes that maintain extracellular matrix (ECM) homeostasis of the organ and store vitamin A in cytoplasmic lipid droplets[7]. During liver homeostasis, HSCs are in a quiescent state, but in response to injury, they activate and acquire a myofibroblastic-like phenotype, participating in the wound-healing response to injury and in tissue regeneration. In chronic liver injury, activation of HSCs persists, and they become the main fibrogenic cell type[8]. Cell metabolism is crucial for the activation of HSCs, which, to fulfil the high metabolic requirements during activation, increases glycolysis[9], glutaminolysis[10] and de novo lipogenesis[11].

The maintenance of the HSCs quiescent phenotype is tightly regulated by transcription factors (TF). Some of these TF are expressed during liver development and become downregulated during HSCs activation[12–14]. Restoration of their expression in activated HSCs, re-establish, in part, the quiescent state, indicating a parallelism between both processes of maturation and fibrogenesis[12–14]. Thus, suggesting that understanding the trajectory of HSCs in development and disease may help to identify molecular pathways suitable for preventing HSCs activation or promoting the regression to a quiescent phenotype, thus mitigating fibrogenesis in chronic liver diseases.

RORA (Retinoic Acid Related Oprhan Receptor Alpha) is a member of the steroid/thyroid hormone receptor superfamily of TFs expressed in several tissues, including the liver, where it is known to regulate genes involved in hepatocyte lipid, cholesterol and glucose metabolism. RORA plays a major role in cellular development and differentiation of multiple tissues[15,16], but its role in HSCs physiology remains poorly explored. Recent studies suggest that RORA may also play a role in the activation process of HSCs[17,18].

In this study, we performed a time-resolving proteome characterization of iPSCs to functional HSCs (diHSCs), which mimic phenotypic and functional characteristics of primary human HSCs. Furthermore, we identified RORA as a TF regulating both diHSCs differentiation and favouring the maintenance of a quiescent phenotype by modulating the metabolic state of the cells. In both, mesoderm commitment and diHSCs activation, downregulation of RORA mediates a metabolic switch, increasing glycolysis and mitochondrial oxidative phosphorylation system (OXPHOS). Moreover, we confirmed the anti-fibrogenic role of RORA in hepatic and extrahepatic pericytes, thus positioning RORA as a potential antifibrogenic multiorgan target. Overall, this work shows the potential of studying cell trajectories along differentiation and disease progression.

Results

Time-resolving proteomic analysis of diHSCs differentiation

To construct a comprehensive proteomic profile of the iPSC differentiation towards functional iPSC-differentiated HSCs (diHSCs), we obtained 7 different timepoints across differentiation (day 0, day 2, day 4, day 6, day 8, day 10 and day 12) as previously described[19–21]. Samples from four independent differentiations were collected and assessed using mass spectrometry (MS)-based profiling (Fig. 1A). We identified 3064 proteins, of which 2475 were quantified, providing a detailed proteomic roadmap of the differentiation process from iPSCs to diHSCs.

As expected, during the differentiation, HSC markers (DCN, LUM, PTN, MMP2, PCOLCE, LAMA5, IGFBP3, LGALS1, IGFBP5, and collagens) increased, accompanied by a decrease in the pluripotency proteins (RIF1, POU5F1, DPPA4, KPNA2, DNMT3B) (Fig. 1B, C). As expected at day 0, we found proteins enriched in gene ontologies (GOs) related to cell proliferation, translation, cell division, and pluripotency. Conversely, at day 12, we observed an enrichment in proteins related to ECM organization, collagen metabolism, wound healing, and TGFβ signaling (Fig. 1B; Supplementary Data 1). Gene Set Enrichment Analysis (GSEA) of proteome signatures of human liver cell types[22] showed that the diHSCs proteome profile was significantly enriched in the HSC proteome signature, closely resembling the human primary HSCs proteome. (Fig. 1D).

Moreover, based on the dynamic proteomic profile, we identified five expression clusters (Supplementary Fig. 1 and Supplementary Data 1); 1) A matrisome-enriched cluster, arising on day 8 and including proteins related to ECM organization and collagen metabolism (Fig. 1E and Supplementary Fig. 1B); 2) A metabolic cluster containing proteins involved in vesicular processes and cell commitment which was up-regulated on days 4-8 and hereafter referred as “met-proteins” (Fig. 1F and Supplementary Fig. 1B); 3) a proliferation- and 4) a pluripotency-cluster, which both contained proteins down-regulated during differentiation (Fig. 1G, H, Supplementary Fig. 1B); and 5) a basal-proteins cluster, containing proteins showing minimal changes at the different stages of the differentiation, and involved in homeostatic cellular processes (Fig. 1I, Supplementary Fig. 1B). Altogether, this broad characterization enabled the construction of a proteomic roadmap detailing the differentiation of diHSCs from iPSCs.

diHSCs resemble human primary HSCs proteome identity

We next evaluated the similarity between diHSCs and primary human healthy HSCs (pHSCs) isolated from liver donors. When comparing the proteomes of diHSCs and pHSCs, we found that over 60% of their profiles were shared (Fig. 1J). Notably, several proteins associated with the activated phenotype were enriched in pHSCs compared to the diHSCs, including EHD2, TIMP3, THY1, TIMP1, MYL9, and FBLN2. These markers suggest that primary HSCs exhibit a more activated state than diHSCs. Interestingly, proteins expressed by diHSCs showed a more proliferative state, reflecting increased cell division and chromatin remodeling, typical of iPSC-derived cells (Fig. 1J). Most importantly, pHSC and diHSCs shared proteins related to ECM remodeling, such as FSTL1, MMP14, SFRP2, PALLD, LOXL2, and RAB13 (Fig. 1J).

Finally, by interrogating our proteomic data with published gene signatures of quiescent, activated, and stellate cell phenotypes (Zhang et al.)[23], we observed that during differentiation, diHSCs gained expression of pathways related to quiescence, activation, as well as HSC identity phenotype (Fig. 1K–M). Overall, these data confirm that iPSCs progressively acquire the stellate proteomic phenotype along differentiation, thus enabling the use of diHSCs to further investigate their role in cell commitment and disease.

Proteome-driven cell trajectory analysis identify RORA as a potential driver of diHSCs differentiation

Principal component analysis (PCA) of the proteome differentiation profile showed a time-dependent distribution of samples along the differentiation process (Fig. 2A). Proteins comprised in PC1 explained stellate cell commitment across time, as cells gained in proteins related to collagen metabolism, ECM organization, or wound healing processes.

To further dissect the progression of the differentiation, we performed Pearson’s correlation analysis showing that proteome data is divided into three phases (Fig. 2B). Phase 1, including days 0 to 2 and characterized by the expression of pluripotency- and proliferation proteins, such as POU5F1 and RIF1 (Fig. 2C), as well as early mesoderm proteins, such as CALB1 and MFGE8. In Phase 2, extended from day 4 to

https://doi.org/10.1038/s41467-025-56024-4

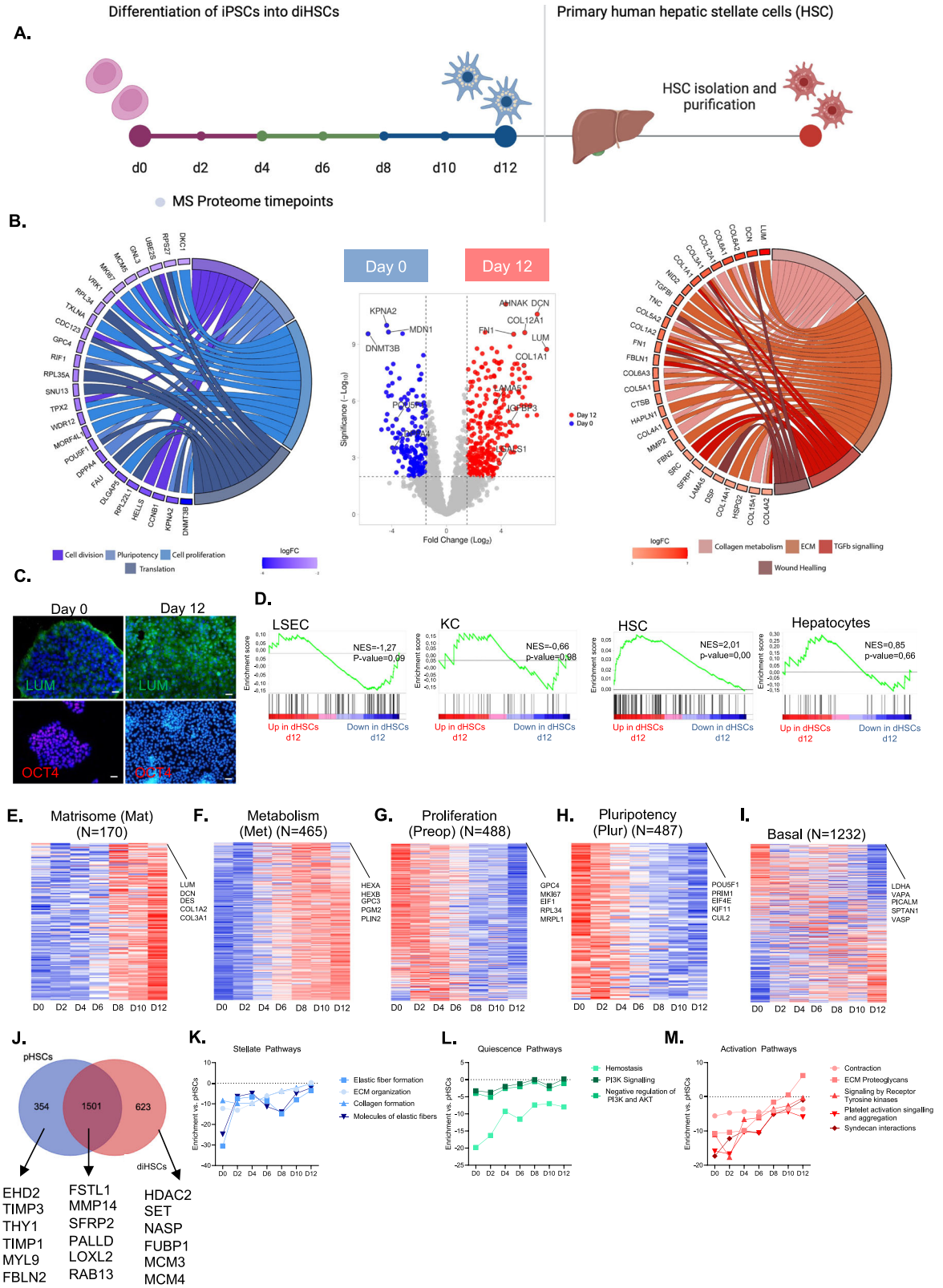

day 6, cells started to express met-proteins together with mesenchymal (FN1, ANXA6, PEF1, and VIM), fetal liver mesothelial proteins (FLNC, KRT18, CGN, and ALCAM), and fetal HSC markers such as COL6A3, NID2, FBLN, and PTN (Fig. 2C). Finally, phase 3, from days 8 to day 12, was characterized by the final mature population of diHSCs, showing enrichment of matrisome-related proteins and mature HSCs proteins including aSMA, COL1A1, DES, and MMP2 (Fig. 2C).

When comparing the proteomic profiles between phases, we observed that proteins differentially expressed from Phase 1 to Phase 2 were related to characteristics of mesenchymal and mesothelial cells such as desmosomes and tight junction formation (DESP, DSG2, PRDX4) (Fig. 2D). Proteins differentially expressed between phases 2 and 3 were related to collagen and ECM organization (COL5A1, LUM, TNC, TGFBI, and NID2), which are typically expressed in HSCs,

Fig. 1 | Time-resolved proteomic characterization of the iPSCs differentiation to diHSCs shows that the stellate cell phenotype is acquired gradually. **A** Schematic representation of the experimental design used to characterize the differentiation process of iPSCs into diHSCs (differentiated hepatic stellate cells) at the proteome level, with a comparison to primary human HSCs. This characterization was performed in four independent differentiations and 4 primary HSCs. Created in https://BioRender.com. **B** Chord diagram illustrating the enriched Gene Ontologies (GOs) at day 0 and day 12 of the differentiation protocol, alongside a volcano plot showing differentially expressed proteins between these two timepoints. **C** Immunoflourescence images at day 0 and day 12, showing the expression of LUM and OCT4. Scale bars: 200 μm for day 0, and 100 μm for day 12. **D** Gene Set Enrichment Analysis (GSEA) of proteomic signatures from different human liver cell types, including LSEC (Liver Sinusoidal Endothelial Cells), KC (Kupffer Cells), HSC (Hepatic Stellate Cells), and HEP (Hepatocytes) obtained from Ölander, M. et al.[22]. **E–I** Protein expression profiles of the five identified clusters during differentiation. The time points are labeled as D0 (day 0), D2 (day 2), D4 (day 4), D6 (day 6), D8 (day 8), D10 (day 10), and D12 (day 12). **J** Venn diagram showing the overlap in proteome profiles between primary HSCs and diHSCs, highlighting the most highly expressed proteins in each cell type including EHD2, TIMP3, THY1, TIMP1, MYL9 and FBLN2 for pHSCs; HDAC2, SET, NASP, FUBP1, MCM3 and MCM4 for diHSCs and as common proteins FSTL1, MMP14, SFRP2, PALLD, LOXL2 and RAB13. (K-M) diHSCs exhibit pathways related to both quiescent and activated phenotypes, as well as key stellate cell pathways identified from the literature (Zhang et al.[23]).

reinforcing the notion that mature HSCs appear in phase 3 of the differentiation (Fig. 2E). These results indicate that the diHSCs differentiation takes place in three main phases, which mimic key stages of embryonic development.

Next, we assessed which TF were involved in the trajectory of HSCs from cell differentiation to cell identity, focusing on those regulating the transition between the identified phases. Our analysis identified RORA as the most significant TF predicted to be regulating the transition between phases 1 and 2, indicating a possible role of RORA in mesoderm commitment (Fig. 2D and Supplementary Data 2). Meis homeobox 1 (MEIS1) was predicted to regulate the transition from phases 2 to 3 (Fig. 2E and Supplementary Data 2). To further explore the role of TFs in stellate cell identity, we compared Phase 3 cells to pHSCs (Fig. 2F and Supplementary Data 2). To ensure the relevance of the selected TF to the pHSCs, we interrogated deposited and publicly available transcriptomic data from quiescent and activated primary human HSCs (GSE90525 & GSE67664)[19]. This analysis confirmed that RORA was the only TF upregulated in both quiescent and activated pHSCs when compared to diHSCs, thus suggesting its potential role in the acquisition the HSCs phenotype (Fig. 2G).

RORA facilitates the diHSCs mature phenotype by improving mesoderm commitment

During diHSCs differentiation, the gene expression of RORA showed a significant increase at day 4 of differentiation and progressively declined at days 6, 8, 10, lowering the pHSCs expression at day 12 (Fig. 3A).

To assess the role of RORA across the differentiation, we activated RORA using the agonist SR1078 from day 2 until the end of the differentiation (day 12) (Fig. 3B). While the RORA agonist did not change the morphology of diHSCs (Supplementary Fig. 2A), we found that it increased the expression of mature HSC markers such as *PCDH7*, *LRAT*, *LHX2* and *RELN* (Fig. 3C). At transcriptome level, the GSEA analysis of gene signatures of quiescent, activated and hepatic stellate phenotype (Zhang et al.[23]), revealed that RORA agonism promoted the quiescent gene signature (NES = 1.82; p-value = 0.024) (Fig. 3D), while preserving the cells' responsiveness to TGFβ (Supplementary Fig. 2B). Moreover, as shown by differential clustering in the PCA (Fig. 3E), RORA agonism induced transcriptomic changes in diHSCs, also reflected by the enrichment in biological processes and markers related to mesoderm (i.e. *EOMES*, *SRF* or *GJA1*) and mesenchyme development (i.e. *GREM1*, *HAS2* or *FGF8*) (Fig. 3F–H) and reduced enrichment in the biological processes related to cell proliferation (Fig. 3F and Supplementary Data 3). Functional transcriptomic analysis of differentially expressed genes in diHSCs treated with RORA agonist, identified enriched Reactome pathways such as FGFs signalling and a reduction of beta-oxidation, tricarboxylic acid (TCA) cycle and mitotic cycle (Fig. 3I and Supplementary Data 3). These findings suggest that RORA plays a pivotal role in regulating cellular metabolism during diHSCs differentiation. Overall, these data indicate that RORA might act as a transcriptional regulator of the mesoderm and mesenchymal specification, facilitating diHSCs differentiation.

Functional role of RORA in mesoderm and mesenchymal specification

To further dissect the role of RORA in diHSCs differentiation, we generated three heterozygous RORA-knockout iPSCs clones (RORA$^{+/-}$) using CRISPR-Cas9 technology thus, mimicking in one allele the mutation presented in staggerer mice (sg/sg), spontaneous KO mice for the RORA gene[24]. Generation of iPSCs RORA$^{+/-}$ was confirmed by Sanger sequencing (Supplementary Fig. 2C). Cells showed a reduction in protein expression of RORA preserving pluripotency markers such as *SOX2*, *OCT4* and *NANOG* at both gene and protein expression (Supplementary Fig. 2D-F). Moreover, all the clones generated presented a normal karyotype, thus confirming the genome stability of the newly generated cell lines (Supplementary Fig. 2G). Interestingly, during the differentiation of RORA$^{+/-}$ iPSCs we observed in all the clones tested with nearly 80% of the cells dying after day 4 (Fig. 3J). To address the cell mortality observed in RORA$^{+/-}$ iPSCs, we treated the cells with the RORA agonist SR1078 from day 2 until the end of differentiation. This treatment successfully reduced mortality in the RORA$^{+/-}$ differentiating cells and allowed cells to progress to the end of the differentiation, showing an HSCs phenotype but with differences in the expression of *LRAT, LHX2, RELN* and *ACTA2* compared to the control WT (Fig. 3J, K). Moreover, RORA$^{+/-}$ diHSCs, showed a higher activation when plated on plastic (Fig. 3L, M).

To bypass the lethality associated with RORA during the early stages of differentiation, we established an inducible doxycycline dependent (iCas9) system, to facilitate downregulation of RORA after reaching the mesoderm phase. To initiate Cas9 expression at the start of stage 3 of differentiation (day 8), we treated the cells with doxycycline starting at day 4 of the differentiation. By day 12, the differentiated cells showed a substantial increase in *CAS9* expression, accompanied by significant upregulation of key stellate cell activation markers, particularly *ACTA2* and *COL1A1*. In contrast, we noted a marked downregulation of *LRAT, RELN*, and *LHX2* (Supplementary Fig. 2H), suggesting the acquisition of a more activated phenotype than control WT cells. These results were confirmed by using a chemical antagonist of RORA (SR1001) in the differentiation of wild type (WT) iPSCs. SR1001 treated cells showed a spindle morphology with increased ECM production at the end of differentiation (Supplementary Fig. 2I-J), while reducing gene expression of the HSCs genes *RELN* and *LHX2* and increasing *COL1A1* and *ACTA2* (Supplementary Fig. 2K), together with increased collagen deposition, as assessed by Picrosirius staining (Supplementary Fig. 2K). Overall, these results position RORA as a potential transcriptional regulator of mesoderm and mesenchymal differentiation and key for the acquisition of the quiescent phenotype of diHSCs.

RORA promotes a quiescent diHSCs phenotype and prevents diHSCs activation

Next, we evaluated the effect of RORA on diHSCs activation and fibrosis using two in vitro models of diHSCs activation, one based on passage and the other based on TGFβ stimuli. Previously we have shown that passaged diHSCs are a good model to induce cell activation

https://doi.org/10.1038/s41467-025-56024-4

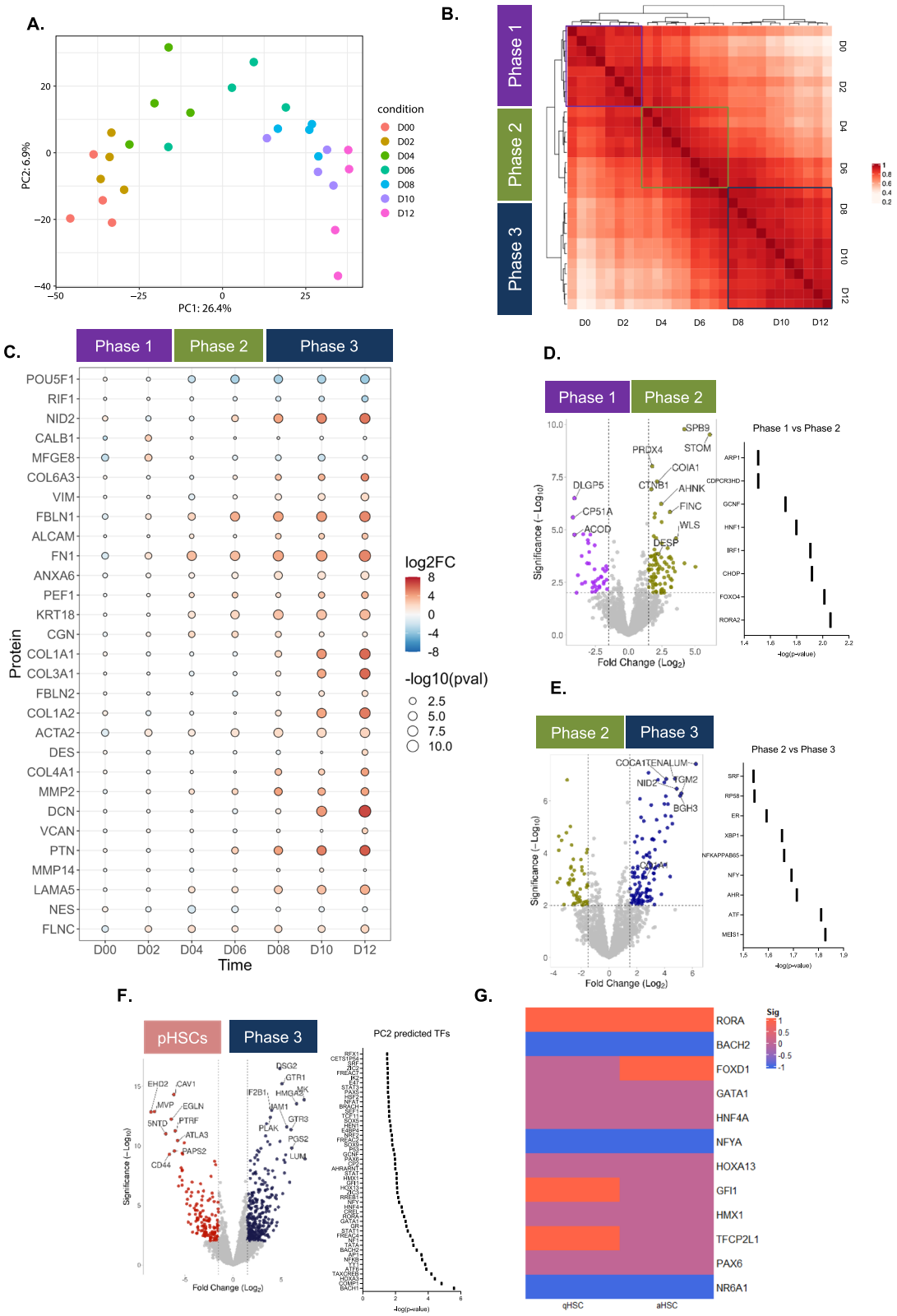

promoting a fibrogenic response[14]. diHSCs derived from WT iPSCs treated with the RORA agonist SR1078 for 24 h, prevented activation of passaged diHSCs and decreased the expression of activation markers *ACTA2* and *COL1A1*, at both gene and protein levels (Fig. 3N, O) while increased the expression of quiescent markers *LHX2* and *LRAT* (Fig. 3O). On the contrary, cells treated with the RORA antagonist (SR1001) after passage, increased their activation profile (Supplementary Fig. 3A).

Transcriptomic analysis of the passaged diHSCs treated with SR1078 showed a reduction in GOs related to de novo lipogenesis and mitochondrial fatty acid β-oxidation (Fig. 3P and Supplementary Data 3). In addition, as shown in Fig. 3P, Q and Supplementary data 3,

Fig. 2 | Proteome trajectory analysis of diHSCs differentiation discovers three stages of maturation and identifies RORA as a potential driver of stellate cell differentiation. A Principal component analysis (PCA) of the proteome during differentiation reveals a time-dependent separation of data, indicating distinct stages of the differentiation process. **B** Pearson correlation analysis identifies three phases of differentiation towards diHSCs: Phase 1 from day 0 (D0) to day 4 (D4), Phase 2 from day 4 (D4) to day 8 (D8), and the final maturation phase (Phase 3) from day 8 (D8) to day 12 (D12). **C** Dot plot showing protein enrichment throughout the differentiation process. In Phase 1 (D0 to D4), pluripotency and mesoderm markers (POU5F1, RIF1, MFGE8, CALB1) are enriched. During Phase 2 (D4 to D8), mesenchymal and mesothelial proteins, along with fetal HSC markers (VIM, PEF1, KRT18, FN1, FBLN1, COL6A3, CGN, ANXA6, ALCAM), begin to dominate. Finally, in Phase 3 (D8 to D12), markers of mature HSCs are enriched (VCAN, PTN, NES, MMP2, MMP14, LAMA5, FLNC, FBLN2, DES, DCN, COL4A1, COL3A1, COL1A2, COL1A1, ACTA2). **D** Volcano plot comparing phases 1 and 2 highlights the enrichment of mesothelial markers (DESP, DSG2, PRDX4, WLS) and transcription factors (TFs) predicted in silico to regulate this transition. **E** Volcano Plot showing the comparison between phases 2 and 3 shows an increase in collagen and extracellular matrix (ECM) proteins (COL5A1, LUM, TNC, TGFBI, NID2), along with predicted TFs modulating this transition. **F** Volcano plot displaying the differentially expressed proteins between phase 3 (diHSCs) and primary HSCs, as well as the in silico predicted TFs involved in regulating the adult hepatic stellate cell phenotype. **G** Transcriptomic comparison of primary human activated and quiescent stellate cells with diHSCs, focusing on the predicted TFs modulating the adult stellate cell phenotype, using data from GSE90525 and GSE67664. Fold change (FC) between diHSCs vs. qHSCs = 3.20; FC diHSCs vs. aHSCs =1.60 for RORA expression.

Reactome analysis showed changes in metabolic pathways, thereby suggesting a remodeling of the metabolic state in the diHSCs to maintain the quiescence phenotype. To evaluate which pathways may be regulated by RORA we investigated which genes were predicted to be direct targets of RORA in the GSEA database. Predicted genes contain at least one occurrence of the motif NWAWNNAGGTCAN within 4 kb of their transcription start sites [-2kb, +2 kb], corresponding to the RORA transcription factor binding site (V$RORA1_01, v7.4 TRANSFAC). Notably, we identified several genes related to differentiation (I*TGAX, NRP1*, and *TSPAN7*) and cytokines or growth factors involved in mesoderm and mesenchymal differentiation (*CALCA, CMTM6, CNTF, CX3CL1, FGF9, IL17, IL22, IL7, NTF3, SEMA3F*). Interestingly, most of these genes were transcription factors, suggesting that RORA functions as a master regulator, integrating diverse biological pathways to coordinate processes such as development, circadian rhythms, cell cycle regulation, stress responses, and differentiation (Supplementary Fig. 3B). Differentiated cells treated with the RORA agonist SR1078 showed enrichment in the signature of predicted genes.

Next, we evaluated the effect of RORA on diHSCs response to TGFβ, as a second activation model[20]. diHSCs were treated with TGFβ for 24 h or 7 days while the SR1078 RORA agonist was added for the last 24 h. diHSCs treated with SR1078 reduced both short and long-term TGFβ-activation by decreasing *ACTA2*, *COL1A1* and *LOX* (Fig. 3R).

To study the effect of RORA in a complex in vitro system, we evaluated the effect of SR1078 in 3D liver spheroids of HepG2 and diHSCs. Incubation of liver spheroids with SR1078 for 24 h reduced the expression of *COL1A1*, *ACTA2* and *LOX* (Fig. 3S). Moreover, liver spheroids incubated with TGFβ and treated with SR1078 also showed a reduced expression of activation markers (*COL1A1* and *ACTA2*) (Fig. 3T) as well. Overall, these results suggest that RORA plays a role in the deactivation of diHSCs and the maintenance of the quiescent diHSCs phenotype, which can be mediated by blocking metabolic adaptations required for HSCs activation.

RORA regulates cell metabolism during mesoderm differentiation and diHSCs activation

Since our data showed that RORA may be responsible for the modulation of the metabolic state of the cells along diHSCs differentiation and activation, we evaluated diHSCs metabolic reprogramming in the presence and absence of RORA, both during differentiation and activation. Previous reports showed that cells exiting pluripotency and differentiating to mesoderm undergo a metabolic switch increasing oxidative phosphorylation (OXPHOS) while reducing glycolytic flux[25]. Similarly, activation of HSCs is dependent upon induction of glycolysis[9], glutaminolysis[10] and de novo lipogenesis[11].

Using the Seahorse real-time cell metabolic analyzer, we found that cells from iPSC-RORA$^{+/-}$ differentiation have increased mitochondrial respiration at day 4, when mesoderm specification occurs just before cell death (basal, ATP-coupled and maximal respiration) (Fig. 4A, B). In addition, adenosine triphosphate (ATP) production from glycolysis was also increased in these cells, (Fig. 4A–C), and have higher intracellular glucose levels (Fig. 4D), suggesting that cells derived from iPSC-RORA$^{+/-}$ retained a metabolic profile more characteristic of undifferentiated cells. Accordingly, iPSC-RORA$^{+/-}$ cells expressed higher levels of genes related to glycolytic flux (*ALDOB* and *GS6P*) and a decreased expression of *ACACA* (Fig. 4E). Moreover, the expression of mesoderm (EOMES) and mesenchymal (VIM) markers was reduced at both protein and gene expression in iPSC-RORA$^{+/-}$ cells at day 4 of the differentiation (Fig. 4E, F) when compared to WT iPSCs. However, when iPSC-RORA$^{+/-}$ cells were treated with RORA agonist, they showed a reduction in intracellular glucose and glycolysis-dependent ATP production (Fig. 4C, D), glycolytic gene expression (Fig. 4E) and glucose consumption from the media (Fig. 4D), thus confirming that iPSC-RORA$^{+/-}$ cells fail to initiate the differentiation toward mesoderm during diHSCs differentiations and retain a glycolytic profile of undifferentiated cells.

To explore the role of RORA in mesoderm commitment, we differentiated iPSC-RORA$^{+/-}$ cells into both non-directed mesoderm, and renal mesoderm using established protocols. Non-directed mesoderm differentiation protocol showed a reduction in αSMA-GATA4 double positive cells after 21-days differentiation protocol indicating a poor mesoderm commitment (Supplementary Fig. 3C). However, the directed differentiation of iPSC-RORA$^{+/-}$ into renal organoids, did not show significant differences in comparison to control WT iPSCs in terms of protein expression (LTL, PDOXL and ECAD) (Supplementary Fig. 3D), therefore suggesting that RORA's influence on mesoderm differentiation may be context-dependent.

In diHSCs activation models, treatment with the RORA agonist (SR1078) reduced mitochondrial respiration, OXPHOS-dependent ATP production, glycolysis-dependent ATP production as well as intracellular glucose (Fig. 4G–J, L–O). Moreover, genes associated with glycolysis and lipid synthesis that were increased with activation, were found to be reduced after treatment with SR1078 (Fig. 4K, P). Altogether, these results indicate that RORA acts as a metabolic modulator in diHSCs trajectory which impacts the phenotype of diHSCs at different stages, including initial cell commitment and the quiescent cell identity at the end of differentiation.

Given the previously established role of RORA in regulating lipid metabolism[26], we further examined the lipidomic profile of passaged diHSCs treated with SR1078. Our findings indicate a shift towards a quiescent-like lipidomic phenotype, by reducing the number of lipids with higher carbon numbers and degree of saturation (Supplementary Fig. 4A). According to bibliography[27] early HSC activation is marked by a reduction in phosphatidylcholines (PCs) and sphingomyelins containing saturated or monounsaturated fatty acids followed by an increase in PCs and dihexosylceramides (Hex2Cer) at later stages. In our analysis, SR1078-treated diHSCs showed a reduction in PCs and triglycerides (TGs), though no changes in HexCer were detected, likely due to the short treatment duration (Supplementary Fig. 4B). We also observed a shift in the PC2 profile, driven by PCs and sphingomyelins with shorter, less unsaturated fatty acid chains (Supplementary

https://doi.org/10.1038/s41467-025-56024-4

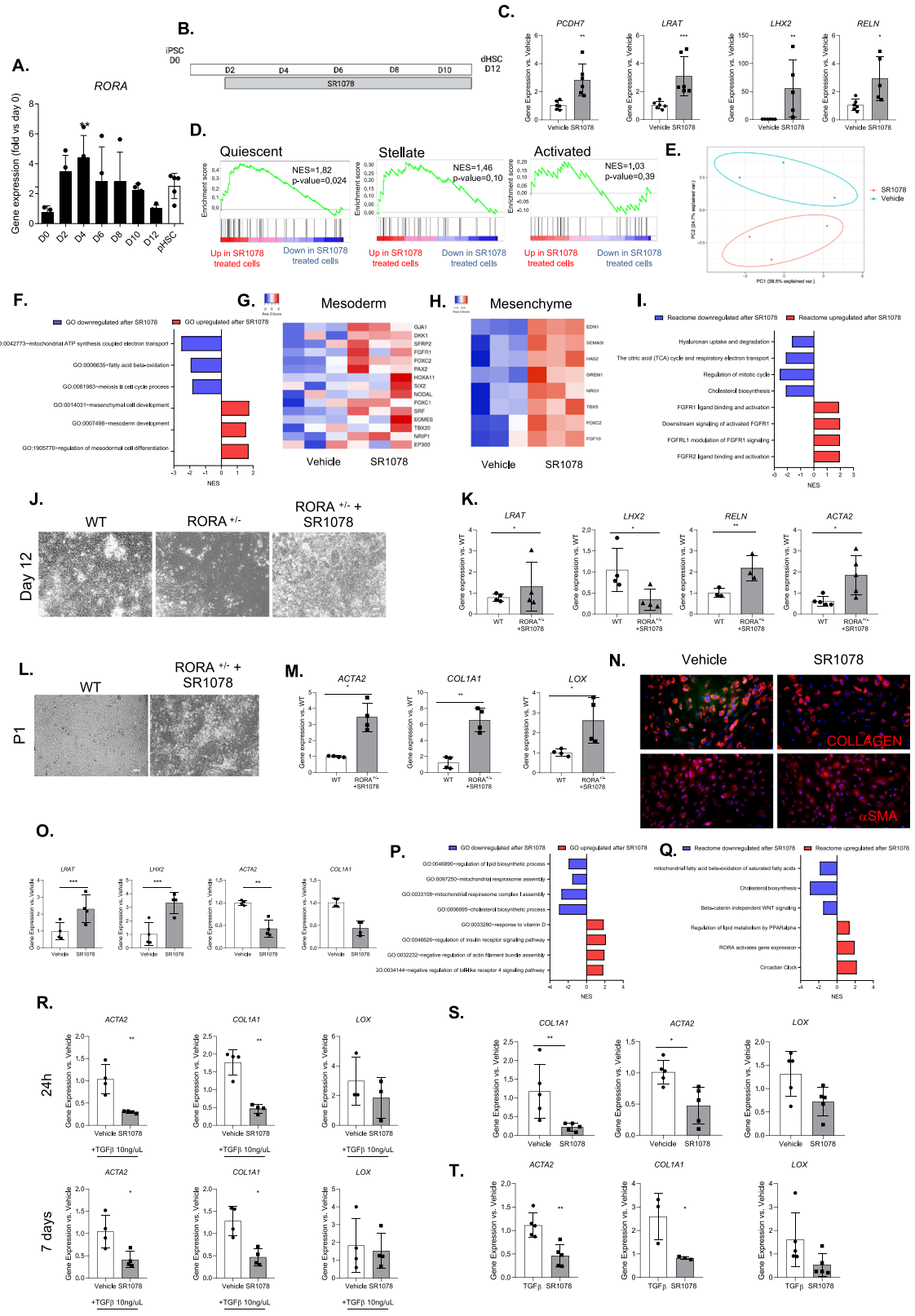

Fig. 4D-E). These findings suggest that RORA agonist treatment promotes a lipidomic profile consistent with quiescent stellate cells.

RORA regulates fibrosis in vivo

To evaluate the role of RORA in HSCs activation and liver fibrosis, we used a RORA-deficient strain, known as staggerer mice, hereafter sg/sg. We found no significant differences in baseline fibrosis of wildtype (WT) and sg/sg livers as shown by the hydroxyproline assay, though sg/sg livers exhibited a slight increase in the expression of *Acta2 and Timp1* activation markers (Supplementary Fig. 5A and B).

Next, we induced liver fibrosis using CCl_4 for 4 weeks (Fig. 5A). The livers of the sg/sg group presented an increased fibrotic content (Picrosirius) coupled with an increased in alpha smooth muscle actin (αSMA) staining as compared to their littermate WT counterparts

Fig. 3 | RAR-related orphan receptor A is a potential driver of the diHSCs phenotype by improving mesoderm commitment and modulating diHSCs activation state. A RORA gene expression during diHSC differentiation compared to primary HSCs (pHSCs). Data represent three independent differentiations and three pHSC samples. Significant differences are indicated as $*p < 0.05$. **B** Schematic of the experimental design for SR1078 treatment during differentiation. Cells were treated with the RORA agonist SR1078 (0.1 mM) from day 2 onwards. **C** Gene expression analysis of key HSC markers (*PCDH7, LRAT, LHX2, RELN*) in three independent differentiations treated with SR1078 compared to the vehicle control. **D** GSEAs of reported gene signatures for quiescent, pan- and activated stellate cells. Obtained from Zhang et al.[23]. **E** Principal Component Analysis (PCA) showing transcriptomic differences between cells treated with the RORA agonist SR1078 from day 2 compared to the untreated group, $n = 3$. **F** GOs upregulated (red) and downregulated (blue) in cells treated with the RORA agonist. **G** Heatmap of mesoderm markers in treated and untreated cells along differentiation with SR1078. **H** Heatmap of mesenchymal markers in treated and untreated cells along differentiation with SR1078. **I** Reactome pathways upregulated (red) and downregulated (blue) in cells treated with the RORA agonist. **J** Representative microscopy images of diHSCs from WT, iPSC- $RORA^{+/-}$ and treated iPSC- $RORA^{+/-}$ with the RORA agonist (SR1078) at day 12. Scale bars represent 100 µm. **K** Gene expression of stellate cell markers (*LRAT, LHX2, RELN* and *ACTA2*) of WT and treated iPSC-$RORA^{+/-}$ with the RORA agonist (SR1078) at day 12. $n = 3$ independent differentiations with two replicates. **L** Representative microscopy images of passaged (P1) diHSCs from WT and iPSC- $RORA^{+/-}$ SR1078 treated. Scale bar represents 100 µm. **M** Gene expression of activated stellate cell markers (*ACTA2, COL1A1 and LOX*). $n = 3$ independent differentiations with two replicates. **N** Immunoflourescence images for COLLAGEN and aSMA in WT passaged cells treated and untreated with RORA agonist SR1078 for 24 h. Scale bars represent 100 µm. **O** Gene expression of quiescent (*LRAT* and *LHX2*) and activated (*ACTA2 and COL1A1*) markers in cells treated with the RORA agonist at passage. $n = 3$ independent differentiations with two replicates. **P** GOs upregulated (red) and downregulated (blue) in treated cells with the RORA agonist at passage. **Q** Reactome pathways upregulated (red) and downregulated (blue) in cells treated with the RORA agonist at passage. **R** Gene expression of activated (markers in cells treated with the RORA agonist at passage, after TGFβ stimulation (10 ng/µL) during 24 h and 7 days. $n = 3$ independent passaged cells with two replicates. **S** Gene expression of activated markers (*ACTA2, COL1A1 and LOX*) in liver spheroids after SR1078 3 mM treatment during 24 h. $n = 3$; Significant differences are indicated as $*p < 0.05$. **T** Gene expression of activated markers (*ACTA2, COL1A1 and LOX*) in liver spheroids after TGFβ stimuli during 24 h and SR1078 3 mM treatment during 24 h more. $n = 3$ independent spheroids experiments with 10 biological pool replicates each; All data is presented as mean ± SEM, no significance or $* p < 0.05$, $**p < 0.01$ was determined by One sample t and Wilcoxon test.

(Fig. 5B). In agreement with previous reports showing increased hepatocyte injury in RORA-KO mice fed with a high-fat diet[26], by hematoxylin and Eosin (H&E) staining we observed an increased tissue damage in the pericentral hepatocytes (Fig. 5B) in the sg/sg group. This was further supported by elevated alanine transaminase (ALT), aspartate transaminase (AST), phosphatase alkaline (AP) and lactate dehydrogenase (LDH) in sg/sg (Supplementary Fig. 5C). Moreover, gene expression of fibrogenic markers such as *Acta2*, *Col1a1*, *Col1a2*, *Timp1* and *Fn1* were significantly increased in the mutant group (Fig. 5C), with an increased neutrophil content (Supplementary Fig. 3D), and no significant differences in macrophages (F4/80) or lymphocytes (CD3) nor in proliferation were observed between groups (Supplementary Fig. 5D).

As *Rora* expression is not limited to HSCs and to clarify RORA's specific involvement in HSC pathophysiology in in vivo context, we generated mice with Rora deficient HSCs. We crossed the $Rora^{fl/fl}$ mice[28] with the LratCre mice[29], generating the heterozygous LratCre-$Rora^{wt/fl}$ offspring, which was used for the experiments. Both LratCre-positive $Rora^{wt/fl}$ (Cre^{+}), and LratCre-negative $Rora^{wt/fl}$ (Cre^{-}) mice, were administered I.P. with CCl4 for 4 weeks. Despite not observing any significant differences in the liver-body weight ratio between the Cre^{+} and Cre^{-} groups (Fig. 5D), we detected a significant downregulation of *Rora* gene expression while maintenance of *Lhx2* (Fig. 5G). Moreover, we observed an increase in collagen deposition in the Cre^{+} vs Cre^{-} group as detected by increased hydroxyproline levels ($p = 0.05$) (Fig. 5E) and enhanced collagen deposition as assessed by Picrosirius staining (Fig. 5F). These changes were accompanied by increased αSMA protein expression (Fig. 5F). Despite these changes in pro-fibrogenic genes and proteins, no significant differences were observed in terms of cell proliferation, as indicated by Mki67 protein expression, nor in the amount of F4/80 positive, and MPO positive cells (Fig. 5X). Altogether, these results confirm the role of RORA during fibrosis in vivo, therefore supporting our in vitro findings and confirming its specific impact on HSC-driven fibrosis.

The RORA agonist reduces liver fibrosis in multiorgan fibrosis models

To explore the translational potential of targeting RORA in fibrogenic diseases, we evaluated fibrotic content and gene expression of *Rora* in different liver disease models (Supplementary Fig. 5E). RORA agonist SR1078 was administered to CCl_4-treated mice (Fig. 6A). SR1078 treatment led to an increase in *Rora* gene expression (Fig. 6B). H&E staining showed reduced tissue damage coupled with reduced collagen deposition and αSMA staining (Fig. 6C). Likewise, we observed a reduced gene expression of fibrogenic and HSCs activation markers such as *Acta2*, *Col1a1*, *Timp1*, *Fn1*, *Col1a2*, *Pparg*, *Mmp2*, *Mmp9*, *Mmp12* and *Timp1* (Fig. 6D and Supplementary Fig. 5A). Immunohistochemistry for F4/80, MPO and CD3 showed a non-significant reduction of inflammatory cell populations in mice treated with SR1078 (Supplementary Fig. 5C). Accordingly, *Il1b*, *Tnfa* and *Il6* inflammatory cytokines gene expression was not significantly reduced (Supplementary Fig. 6A). Moreover, we also detected reduced parenchyma liver damage in SR1078 treated mice, as shown by reduced ALT, AST and LDH serological levels in the SR1078 treated group, compared to the vehicle one (Supplementary Fig. 6B). We also found reduced proliferative activity in the liver parenchyma as shown by mKi67 staining upon SR1078 treatment (Supplementary Fig. 6C). These results suggest that the RORA agonist mitigates liver damage and fibrosis by reducing HSCs activation.

Since HSCs are liver pericytes showing important phenotypic and functional similarities with pericytes from other organs and participating in wound healing response, we also evaluated the effect of RORA agonism in other organs, in extrahepatic wound healing response models. First, we tested the effect of the SR1078 RORA agonist in an isoproterenol-induced cardiac hypertrophy mice model (Fig. 6E). Upon SR1078 treatment, mice showed reduced cardiac expression of *Rora*, accompanied by increased cardiac fibrosis (Fig. 6G). Treatment with the RORA agonist (SR1078) promoted the expression of *Rora* and reduced cardiac fibrogenic genes (*Col3a1* and *Acta2*) (Fig. 6H) as well as ECM deposition as assessed by Masson's trichrome and picrosirius staining (Fig. 6F). Echography analysis showed no differences in cardiac structure and function between the vehicle and the treated group (Table 1). Moreover, RORA treatment did not alter cardiomyocyte hypertrophy as shown by no differences in either the expression levels of the hypertrophy marker *Acta1* nor in the cardiomyocyte area (Supplementary Fig. 6D), suggesting a positive effect of RORA agonism against cardiac fibrosis independently of hypertrophy development.

The antifibrogenic role of RORA was further confirmed using primary culture of neonatal cardiomyocytes (NCMs) and fibroblasts (NCFs). Cultured NCFs to passage 3 reduced *Rora* expression while increasing *Acta2*, while RORA treatment reduced this expression, confirming its anti-fibrogenic effect (Fig. 6I). By contrast, in NCMs, the RORA agonist did not alter cardiomyocyte area or the expression levels

https://doi.org/10.1038/s41467-025-56024-4

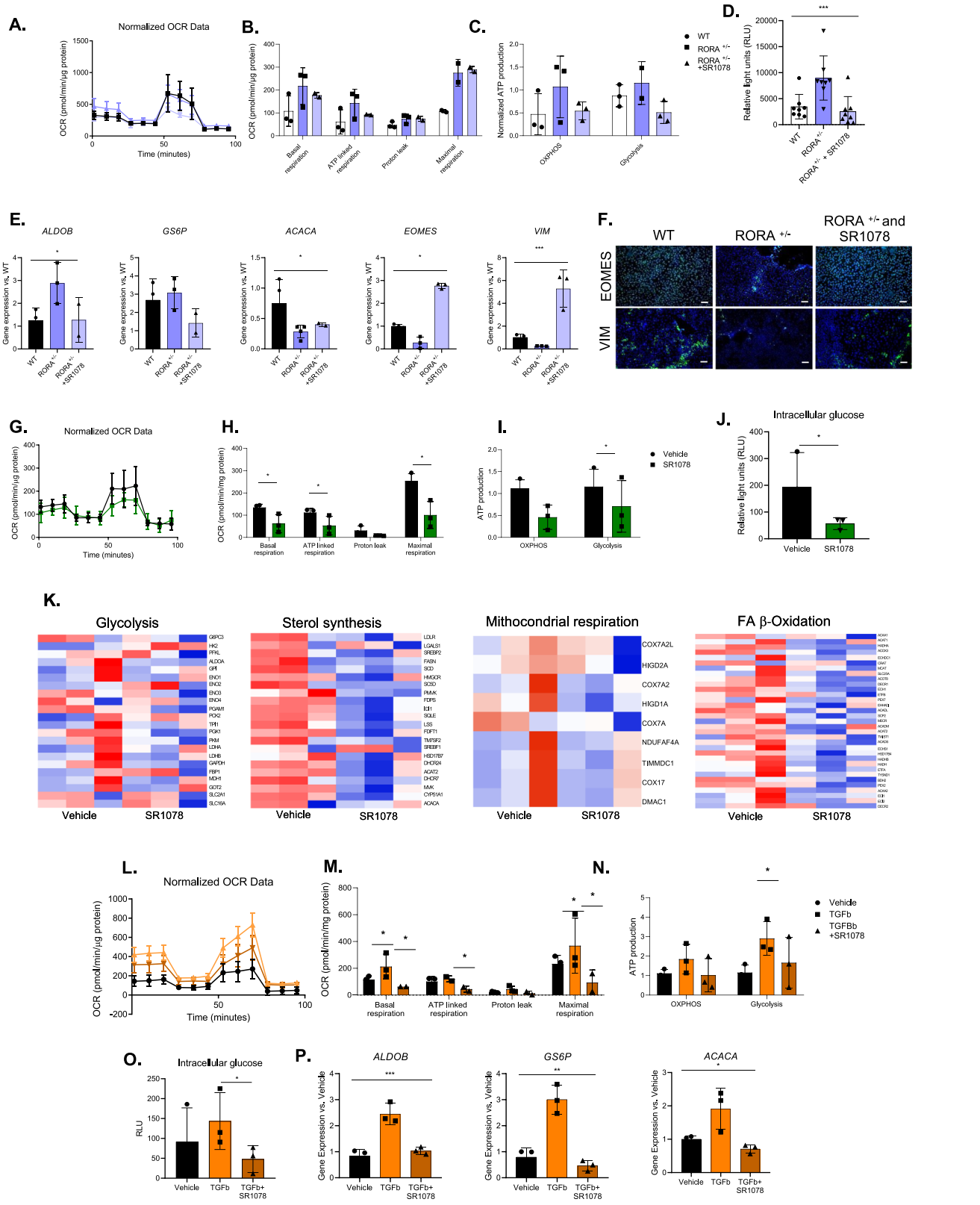

of the *Acta1* hypertrophy marker in the presence of the hypertrophic agent phenylephrine (PE) confirming the absence of anti-hypertrophic effects in vitro (Fig. 6J).

Second, we explored the antifibrogenic potential of RORA in a kidney damage model based on a unilateral ureteral obstruction (UUO) intervention (Supplementary Fig. 6D). The UUO model reduced the expression of *Rora* and promoted kidney fibrosis (Supplementary Fig. 6E). The RORA agonist-treated group showed a reduction in hydroxyproline content, indicating a reduction in collagen deposition (Supplementary Fig. 6F), however, we did not observe any significant reduction of αSMA expression in the 2 groups (Supplementary Fig. 6G). Consistently, SR1078 treated mice, showed a non-significant reduction in the gene expression of *Acta2* and *Col1a1* and an increased expression of *Rora* (Supplementary Fig. 6H).

Fig. 4 | RORA regulates cell metabolism during mesodermal differentiation and diHSCs activation. A Oxygen consumption rate (OCR) on day 4 WT control iPSC and iPSC RORA$^{+/-}$ treated and untreated from day 2. n = 3 independent. (B) OCR parameters of day 4 iPSC WT and iPSC RORA$^{+/-}$ treated and untreated from day 2. *n* = 3 independent differentiations. **C** Normalized adenosine triphosphate (ATP) production from OXPHOS and glycolysis of day 4 WT iPSCs and iPSC-RORA$^{+/-}$ treated and untreated from day 2. *n* = 3 independent differentiations. **D** Glucose consumption at day 4 of WT iPSC and iPSC RORA$^{+/-}$ differentiations treated and untreated from day 2. n = 3 independent differentiations. **E** Gene expression of key glycolytic and lipid synthesis markers (*ALDOB*, *GS6P*, *ACACA*) and mesoderm and mesenchymal markers (*EOMES* and *VIM*). *n* = 3 independent differentiations. **F** Immunofluorescence of mesoderm (EOMES) and mesenchymal (VIM) on day 4 of differentiated cells from WT, RORA$^{+/-}$ and RORA$^{+/-}$ treated with the RORA agonist from day 2. Scale bars represent 100 µm. **G** OCR passaged diHSCs treated with the RORA agonist for 24 h. *n* = 3 independent. **H** OCR parameters of passaged diHSCs treated with the RORA agonist for 24 h. *n* = 3 independent experiments. **I** Normalized ATP production from OXPHOS and glycolysis of passaged cells treated and untreated with RORA agonist for 24 h. *n* = 3 independent differentiations. **J** Glucose consumption at passaged cells treated and untreated with RORA agonist for 24 h. n = 3 independent experiments. **K** Heatmap of glycolytic, sterol synthesis, mitochondrial respiration and fatty acid beta-oxidation of passaged cells treated and untreated cells with RORA agonist for 24 h. *n* = 3 independent experiments. **L** OCR of passaged cells treated with TGFβ 10 ng/mL for 24 h and rescued with RORA agonist treatment for 24 h more. *n* = 3 independent passaged cells. **M** OCR parameters of passaged cells treated with TGFβ 10 ng/mL for 24 h and rescued with RORA agonist treatment for 24 h more. *n* = 3 independent experiments. **N** Normalized ATP production from OXPHOS and glycolysis of TGFβ activation model rescued with the RORA agonist for 24 h. *n* = 3 independent experiments. **O** Intracellular glucose levels of TGFβ activation model rescued with the RORA agonist for 24 h. *n* = 3 independent differentiations. **P** Gene expression of key glycolytic and lipid synthesis markers (*ALDOB*, *GS6P* and *ACACA*) of the TGFβ activation model rescued with the RORA agonist for 24 h. *n* = 3 independent differentiations; All data is presented as mean ± SEM, no significance or * $p < 0.05$, ** $p < 0.01$ was determined by One sample t and Wilcoxon test in one two one comparisons and ANOVA 1-way test was performed in the comparison of three experimental groups.

These results indicate that pharmacological activation of RORA is a promising strategy to mitigate fibrosis in multiple organs, demonstrating the therapeutic potential of targeting RORA to control fibrogenesis.

RORA gene expression negatively correlates with human liver fibrosis

Finally, to evaluate the clinical relevance of our findings, we evaluated RORA expression in cirrhotic patients, and we found that RORA protein and gene expression were both reduced in liver tissue from cirrhotic patients compared to controls (Fig. 7A, B). Moreover, RORA is co-expressed with mesenchymal markers (VIM and αSMA) in healthy and cirrhotic patients (Fig. 7A). Similarly, HSCs isolated from cirrhotic patients showed lower RORA expression than quiescent HSCs (FC = -1,88, *p* value = 0,02) (Fig. 7C), consistent with our data showing RORA loss during HSCs activation. Next, we evaluated the correlation of RORA gene expression with fibrosis in a cohort of patients with different stages of chronic liver disease[30]. RORA gene expression was decreased in patients with Metavir F1-4 (Fig. 7D) and correlated with the FIB4 fibrosis score (Fig. 7E). Moreover, *RORA* expression negatively correlated with the expression of HSC activation and fibrogenic markers such as *ACTA2*, *COL1A1*, *LOXL1*, *TIMP1*, *VEGFC* and *TAGLN* (Fig. 7F).

Discussion

In this study, we aimed to understand the differentiation trajectory of hepatic stellate cells (HSCs) from iPSCs to mature phenotype, leading to the identification of key molecular drivers for diHSCs identity and activation. Understanding HSCs paths in differentiation and activation is essential to delineate how cells acquire their phenotype and how this is lost during disease, thereby providing pathophysiological insights for the development of novel anti-fibrogenic treatments.

While animal models have advanced our understanding of disease progression, translating these findings to humans remains complex, and embryonic differentiation trajectories are difficult to fully capture. Human iPSC differentiation protocols offer a valuable alternative, enabling the study of dynamic cell paths during differentiation, normal physiology, and disease states.

In this article, we performed a time resolving proteomic characterization of the differentiation of diHSCs, leading to the identification of a unique protein signature of this differentiation. Indeed, the comprehensive proteomic data generated in this study will be a useful resource for researchers interested in understanding different aspects of the biology of human HSCs and fibrosis.

We observed a major molecular switch from pluripotency to differentiated cells, where proteins associated with pluripotency and proliferation were downregulated, while proteins characteristic of HSC function were upregulated. During diHSCs differentiation we detected stage-specific markers reportedly expressed at different phases of the embryonic development of HSCs. In this regard, we showed that diHSCs differentiation occurs in three main maturation stages, sequentially expressing markers of mesoderm, mesothelial and immature HSCs. Indeed, the trajectory of diHSCs recapitulates the expression of protein markers described in the embryonic development of HSCs such as ALCAM, ANXA6, CGN, NES or DES[3]. Unfortunately, we lacked a detailed understanding of the human development of HSCs, and therefore we cannot ensure that diHSCs differentiation is faithfully recapitulating all the features and the natural path of the human embryonic development

One of the reasons behind the poor maturation of iPSC-derived cells is the divergence between primary cell development and iPSC-differentiation, which frequently deviate from the natural development path after embryonic stages, thus preventing the maturation of cells[31]. In our study, we identified the role of RORA as a key transcriptional regulator involved in the mesoderm and mesenchymal specification of the cells and in the maintenance of their quiescent phenotype[31]. Moreover, while deletion of RORA impairs early-stage differentiation, the activation of RORA improved diHSCs phenotype. Therefore, our study aligns with the notion that improving the intermediate specification steps of differentiation protocols may be a useful strategy to generate more mature adult cells. Our diHSCs trajectory study during differentiation, also highlights the expression of TF known to regulate HSCs biology and activation such as MEIS1, whose role remains unknown in HSC development but has been described to participate in the activation of HSCs[32].

Moreover, the trajectory analysis of diHSCs differentiation also identified RORA as a key regulator of diHSCs identity and quiescence. The diHSCs derived from iPSC-RORA$^{+/-}$, showed an increased activation phenotype. Furthermore, pharmacological activation of RORA in vitro in diHSCs and in vivo multi-organ fibrosis mouse models showed that activation of RORA prevents pericyte activation and fibrosis. In agreement with these results, we also found that a reduction in RORA gene expression levels, correlates with progression of liver fibrosis, as analyzed in publicly available cohort of patients affected by chronic liver disease[30]. Altogether, our results indicate that RORA is not only implicated in diHSCs differentiation and maturation, but also in HSC activation, where it prevents its brogenic response.

Only few reports have addressed the role of specific TFs in regulating HSCs activation during embryo development. Within the described TF, Both *Tcf21* and *Lhx2* have been shown to be expressed during the embryonic development of the liver, and their expression in HSCs has been described to be downregulated in activation and

https://doi.org/10.1038/s41467-025-56024-4

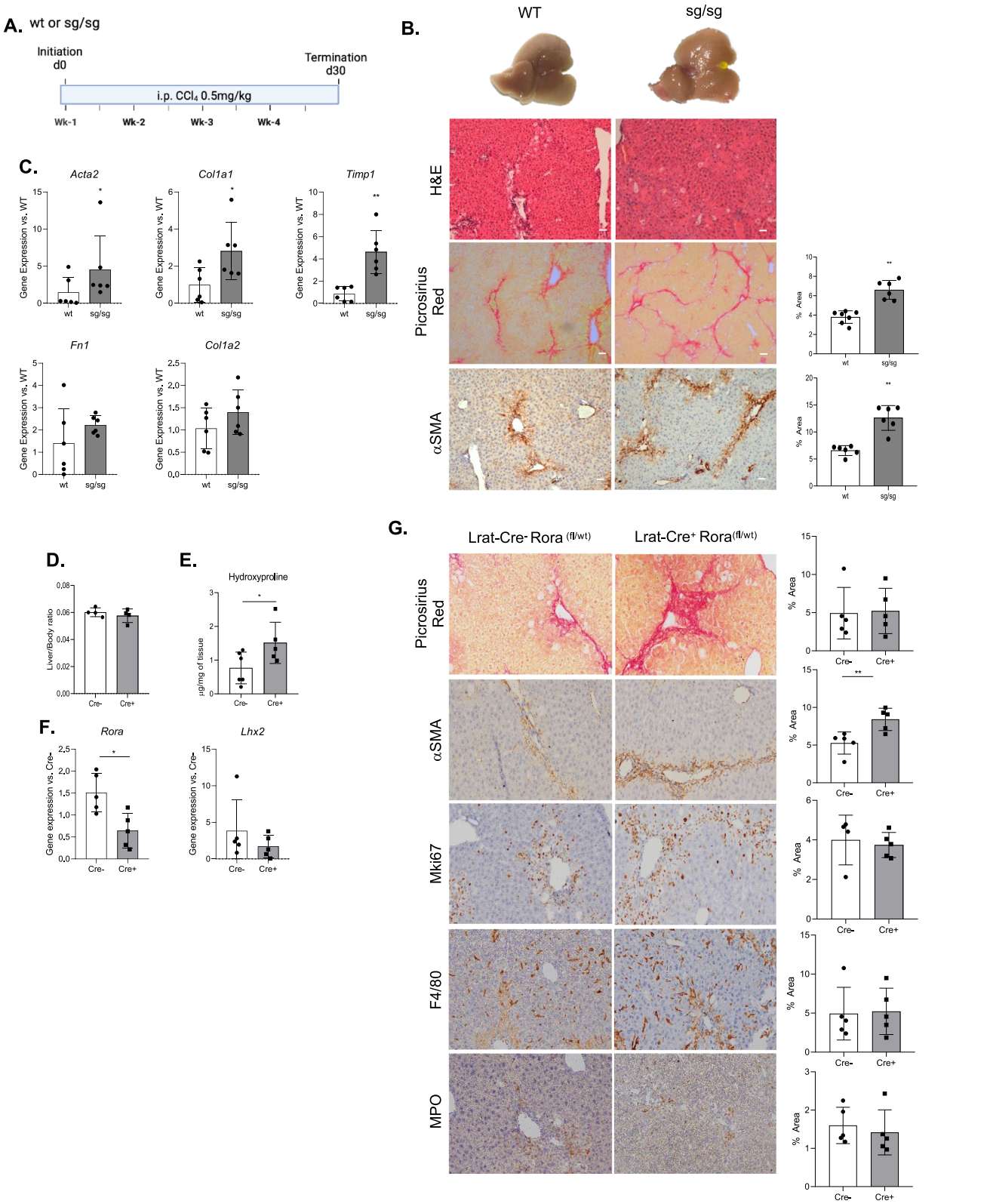

Fig. 5 | RORA controls the activation of HSCs and contributes to the development of liver fibrosis. A Schematic overview of a CCl_4 fibrotic liver model in staggerer mice. (B) Representative images of the livers in 7 staggerer (sg/sg) and 7 WT mice after 4 weeks of CCl_4 treatment, H&E staining and picrosirius staining for the staggerer and wildtype (WT) counterparts and immunohistochemistry of αSMA. Scale bars represent 100 µm. **C** Gene expression of fibrogenic and HSCs activation markers (*Acta2, Col1a1, Timp1, Fn1* and *Col1a2*) in 7 sg/sg and 7 WT mice after CCl_4 treatment. Significant differences are indicated as $^*p < 0.05$. **D** Liver/body ratio of 5 Lrat-Cre-/Rora wt/fl (Cre-) mice vs 5 Lrat-Cre + /Rora wt/fl (Cre +) after 4 weeks of CCl4 I.P. injections. **E** Hydroxyproline content of the livers of 5 Cre- and 5 Cre+ mice after 4 weeks of CCl4 I.P. injections. **F** Gene expression of *Rora* and *Lhx2* in 5 Cre- and 5 Cre+ after 4 weeks of CCl4 I.P. injections. **G** Representative images of the livers of the five Cre- and five Cre+ mice after 4 weeks of CCl4 I.P. injections of picrosirius staining, immunohistochemistry of αSMA, MKi67, F4/80 and Mpo. Scale bars represent 200 µm. All data is presented as mean ± SEM, no significance or $^*p < 0.05$, $^{**}p < 0.01$ was determined by One sample t and Wilcoxon test.

https://doi.org/10.1038/s41467-025-56024-4

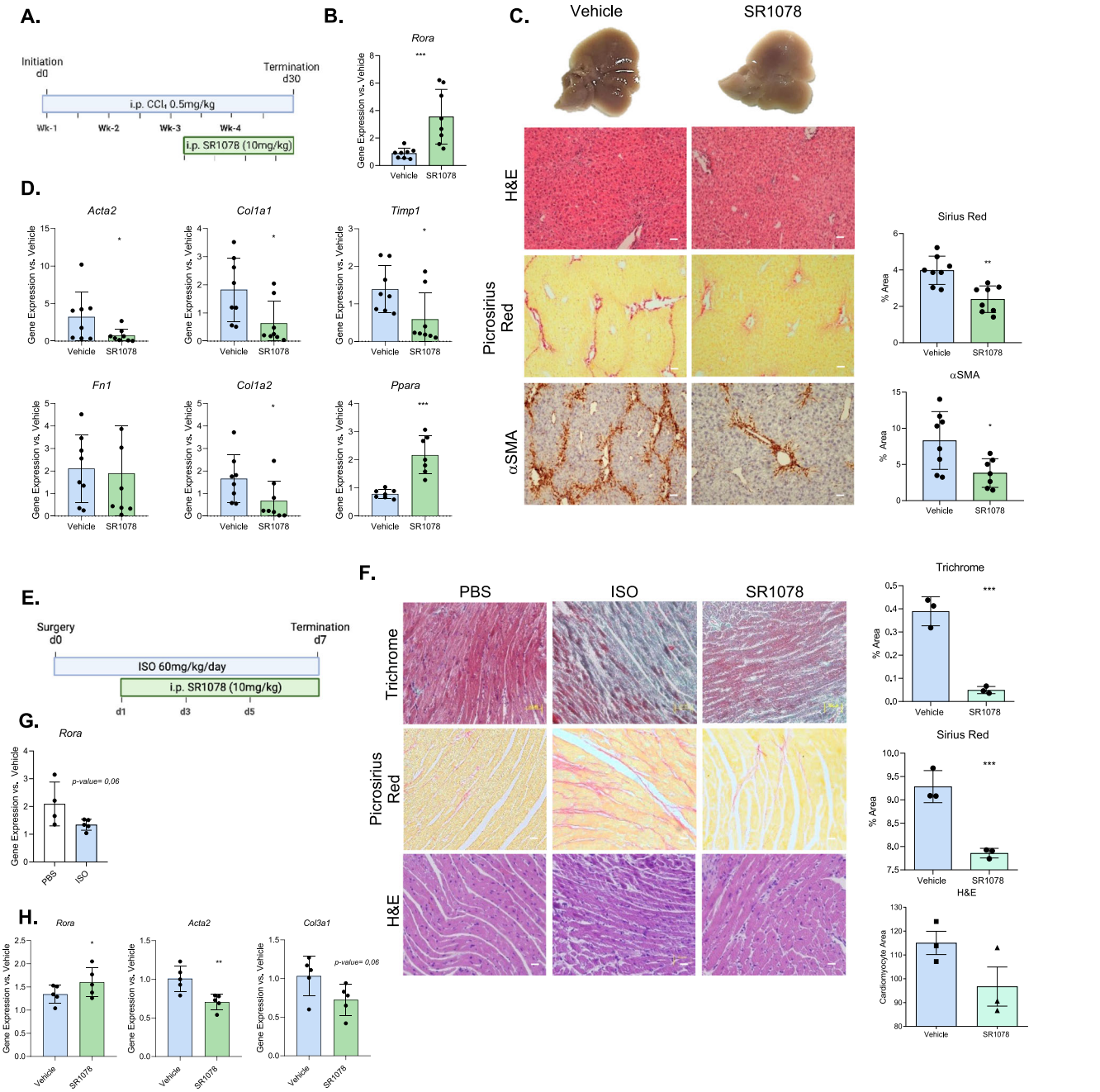

Fig. 6 | diHSCs trajectory analysis is a reliable technique for finding anti-fibrogenic targets. A Illustration of the experimental design of a CCl_4 model treated with SR1078. **B** RORA gene expression of CCl_4 model treated with SR1078; $n = 14$. **C** Representative images of the livers after 4 weeks of CCl4 I.P. injections and SR1078 for the last two, H&E staining and Picrosirius staining for the untreated (Vehicle) and treated (SR1078) group and immunohistochemistry of αSMA. Scale bars represent 100 µm. **D** Gene expression of fibrogenic and HSCs activation markers in 7 untreated (Vehicle) and 7 treated (SR1078) mice (*Acta2, Col1a1, Col1a2, Timp1* and *Fn1*). **E** Illustration of the experimental design of Isoproterenol cardiac injury model performed in two groups of 5 mice each. **F** Representative images of the hearts of vehicle (5 mice), isoproterenol (ISO) (5 mice) and ISO and RORA agonist (5 mice) group of Masson's trichrome, Picrosirius and H&E staining. Scale bars represent 100 µm. **G** *Rora* gene expression of 5 vehicle mice and 5 ISO mice group. **H** Gene expression of *Rora* and fibrogenic markers (*Acta2* and *Col3a1*) and the hypertrophy marker *Acta1* in 5 ISO mice and 5 ISO and RORA agonist mice group. All data is presented as mean ± SEM, no significance or * $p < 0.05$, ** $p < 0.01$ was determined by One sample t and Wilcoxon test.

fibrosis[12–14]. Although their role at the different stages of HSCs maturation is not totally understood, these observations are consistent with our findings, where we also find RORA upregulated at initial stages of differentiation and downregulated during activation, suggesting that they may play a role throughout development and disease. This highlights the potential of iPSC-differentiation approaches for investigating cell trajectories and diHSCs are therefore a powerful tool that may be useful for better understanding the molecular drivers of cell differentiation and disease.

ChIP-Seq analysis of RORA would have been valuable for further insights, but despite efforts suboptimal antibody quality for these assays or inefficient capture prevent the analysis.

Being fibrosis an evolutionary conserved mechanism adopted by different organs in response to chronic injury, here we also aimed at

https://doi.org/10.1038/s41467-025-56024-4

Table 1 | Echocardiographic data from WT animals treated with the RORA agonist (SR1078) after isoproterenol-induced hypertrophy

	ISO (n = 5)				ISO + SR1078 (n = 5)				
	Mean	SEM	vs PBS	Sign.	Mean	SEM	vs PBS	vs ISO	Sign.
Weight (g)	2706	0,9064215	0,9981	n.s.	2954	0,7865113	0,0672	0,0744	+, &
HW/TL (mg/mm)	8,60	0,4770525	0,0368	*	8,42	0,2165247	0,0861	0,9206	*
HW/BW (mg/g)	5,35	0,1742112	0,0045	**	5,11	0,0602953	0,0350	0,5047	*
IVSd (mm)	1,09	0,0209603	<0,0001	****	1,09	0,0184511	<0,0001	>0,9999	****
LVPWd (mm)	1,06	0,0474225	0,0137	*	1,01	0,0521898	0,0406	0,8199	*
LVIDd (mm)	3,71	0,0605677	0,0212	*	3,76	0,1336978	0,0427	0,9186	*
IVSs (mm)	1,66	0,0556677	<0,0001	****	1,67	0,0600518	<0,0001	0,9932	****
LVPWs (mm)	1,60	0,0473216	<0,0001	****	1,63	0,0748287	<0,0001	0,9303	****
LVIDs (mm)	2,41	0,1333642	0,0252	*	2,26	0,2054183	0,0071	0,7655	**
EF (%)	7060	4,0570926	0,1154	n.s.	7533	5,4272973	0,0281	0718	*
FS (%)	3520	3,0177254	0,1647	n.s.	3967	4,6163959	0,0324	0,6192	*
EDV (mm3)	5878	2,2516137	0,0162	*	6095	5,0470108	0,0361	0,8969	*
ESV (mm3)	2075	2,7616187	0,0121	*	18,30	4,1936443	0,0047	0,8607	**
H/R	0,58	0,0404951	0,0019	**	0,53	0,0234068	0,0117	0,5768	*
SI	1,85	0,480944	0,8599	n.s.	2,12	0,0677217	0,9875	0,7793	n.s.
LVm (%)	139,38	6,574084	0,0199	*	137,75	8,9609471	0,0154	0,9887	*
Heart rate M-Mode (bpm)	459,00	22,209107	0,9639	n.s.	448,47	32,204486	0,8703	0,9575	n.s.
Aortic peak (m/s)	0,92	0,0396008	0,3752	n.s.	0,89	0,030991	0,6657	0819	n.s.
VTI (cm)	4,57	0,3096593	0,4143	n.s.	5,18	0,313156	0,0582	0319	+
E peak (m/s)	0,77	0,0415478	0,8924	n.s.	0,78	0,0679918	0,9377	0,9905	n.s.
Mitral deceleration (m/s)	4407	7,6240846	0,8890	n.s.	4087	7,4629455	0,9787	0,9492	n.s.
Aortic diameter (mm)	1,61	0,0254864	0,0951	+	1,72	0,0370885	0,0022	0,0529	**, &
SV (uL)	3803	2,2564999	0,7970	n.s.	4265	4,0387606	0,2859	0,5298	n.s.
CO (mL/min)	169,44	9,4564099	0,5370	n.s.	165,39	11,289067	0,6928	0,9498	n.s.

LVIDd, Left Ventricular Internal Diameter during diastole; *LVIDs*, Left Ventricular Internal Diameter during systole; *IVSd*, Internal Ventricular Septum diameter during diastole; IVSs, Internal Ventricular Septum Diameter During Systole; *LVPWd*, Left Ventricular Posterior Wall thickness diameter during diastole; *LVPWs*, Left Ventricular Posterior Wall thickness diameter during systole. *EDV*, End-Diastolic Volume; *ESV*, End-Systolic Volume; *EF*, Ejection Fraction; *FS*, Fractional Shortening; *H/R*, ventricular thickness/radius; *IE*, sphericity index; *LVm*, Left Ventricular mass; *VTI*, Velocity Time Integral; *SV*, Stroke Volume; *CO*, Cardiac Output.

exploring the presence of potential core fibrosis programs through different organs, and specifically the role of RORA agonism in liver, hearth, kidney fibrosis[33]. A core feature of fibrosis is the activation of fibrogenic cells, such as fibroblasts and myofibroblasts, which undergo significant metabolic changes during activation. Our data suggest that diHSCs serve as a model for pericytes in other tissues, and that RORA regulates pericyte activation in multiple organs, making it a promising therapeutic target for anti-fibrogenic treatments.

As the Metabolic reprogramming is key for the correct embryonic development as well as for cell adaptation to stress or injury, here we also explored how RORA affects diHSCs metabolism through differentiation and disease. During mesoderm differentiation there is a metabolic switching that impairs the glycolytic flux towards a higher OXPHOS[34]. Similarly, activated myofibroblasts, including HSC in the liver, have been described to require a higher energetic demand during activation, mainly due to their increased proliferation, secretion of ECM, proteases and cytokines[35]. Using Transcriptomic data of activated diHSCs treated with the RORA agonist, here we showed a metabolic remodeling of the cells upon treatment, as they decreased beta-oxidation of lipids and glycolytic flux. For instance, fatty acid beta-oxidation is an important energy source for HSCs undergoing activation, as inhibition of mitochondrial fatty acid catabolism blocks HSC activation[36]. Moreover, acetyl-CoA carboxylase (ACC), a regulator of fatty acid beta-oxidation and de novo lipogenesis, has been implicated in HSC metabolic reprogramming during activation[11]. Indeed, in cells treated with the RORA agonist, ACC gene expression decreased, therefore suggesting a downregulation in fatty acid production. Furthermore, diHSCs treated with SR1078 shifted their lipidomic profile towards a more quiescent phenotype, thus, confirming the role of RORA in regulating lipid metabolism in diHSCs. Moreover, using two in vitro models we found that activated diHSCs, showed an increase in OXPHOS and glycolytic flux as compared to the cells treated with RORA agonist, thus reducing the metabolic requirements of the diHSCs and preventing their activation. In addition, our results showed similar results at early stages of differentiation, as iPSC-RORA$^{+/-}$ presented a metabolic profile characteristic of undifferentiated cells that was modified when treated with the RORA agonist, indicating that RORA regulates the metabolic activity during early stages of differentiation, promoting mesoderm differentiation. These results indicate that metabolic flexibility is essential throughout the diHSCs differentiation trajectory and impairs the final phenotype of the cell. This metabolic regulation is mediated in part by RORA as alterations in RORα transcriptional activation are implicated in modulating the cellular physiological state. Our study proposes that changes in RORA expression levels are one of the underlying causes of the observed metabolic state alterations in HSCs and therefore is responsible for the repression of activation, being a potential target for anti-fibrogenic therapy. In conclusion, our study underlines the importance of examining cell trajectories during both differentiation and disease. We show that HSC differentiation and fibrosis mechanisms can be effectively modeled using iPSC-derived cells, thus, enabling the identification of key transcription factors like RORA that regulate cell identity,

https://doi.org/10.1038/s41467-025-56024-4

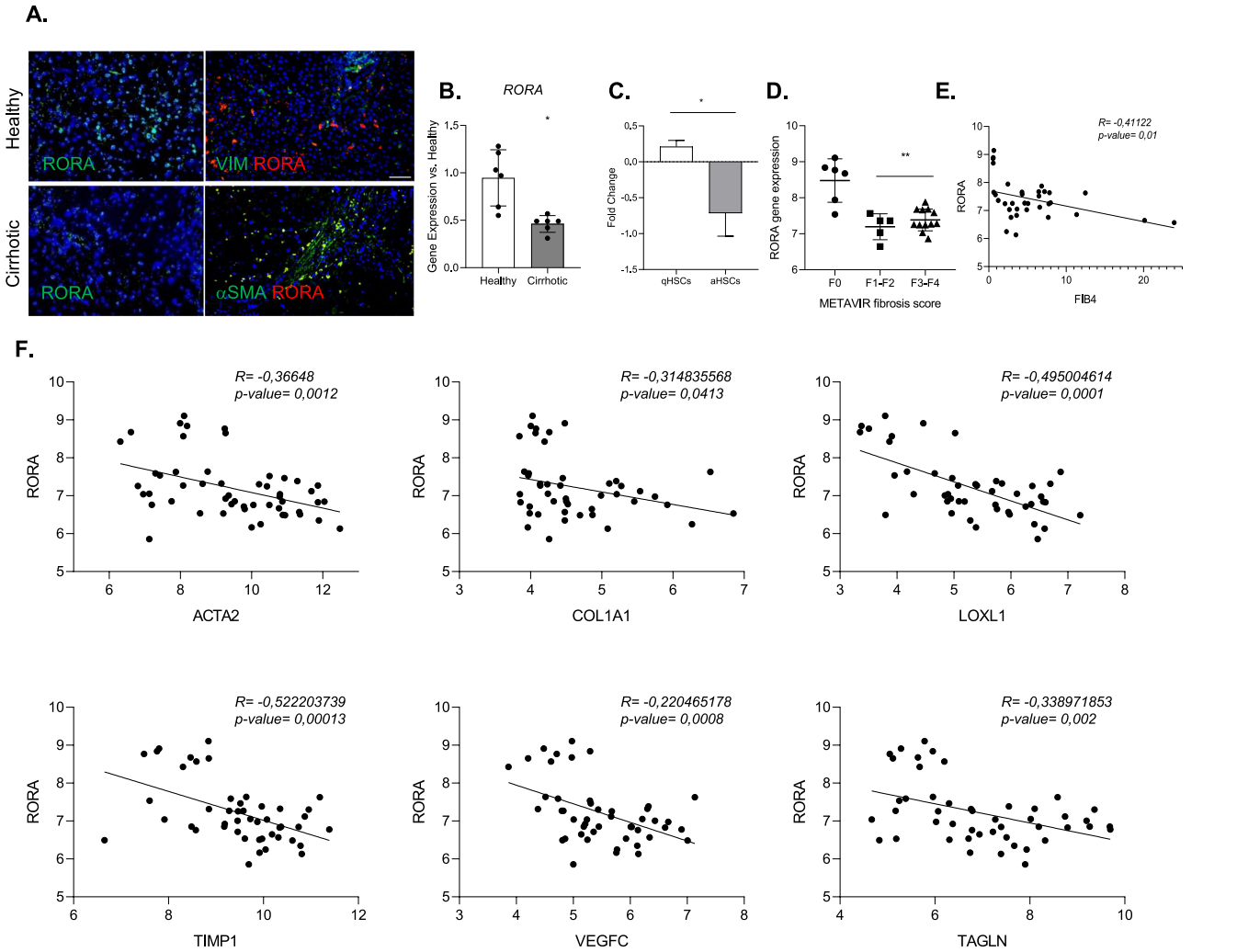

Fig. 7 | RORA is downregulated in a cohort of patients with liver disease and is negatively correlated with liver fibrosis. A Immunoflourescence of RORA in healthy and cirrhotic patients and co-staining of RORA with VIM in healthy and with aSMA in cirrhotic patients. Scale bars represent 100 µm. **B** Gene expression of RORA in cirrhotic patients is reduced in comparison to healthy group. Six total healthy livers and six cirrhotic livers were. **C** Expression of RORA is reduced in primary activated HSCs in comparison to quiescent HSCs (GSE90525 & GSE67664). $n = 4$ samples per condition. **D** RORA expression correlates negatively with METAVIR fibrosis score in a cohort of liver disease patients; $n = 42$ (Graupera et al.[30]). Significant differences are indicated as $*p < 0.05$. **E** RORA expression correlates negatively with FIB4 fibrosis score in a cohort of liver disease patients; $n = 42$ (Graupera et al.[30]). **F** RORA correlates negatively with HSCs activation markers and fibrosis markers (*ACTA2, COL1A1, LOXL1, COL1A1, TIMP1, VEGFC* and *TAGLN*) in a cohort of liver disease patients (Graupera et al.[30]). Gene expression data is presented as mean ± SEM, no significance or $* p < 0.05$, $**p < 0.01$ was determined by One sample t and Wilcoxon test. Correlation analysis data was performed using pearson correlation analysis.

differentiation, and fibrogenesis and can lead to the development of new therapeutic strategies to mitigate fibrosis across multiple tissues.

Methods

Experimental models and subject details

iPSCs cell line For the proteome characterization and all the subsequent in vitro assays, we have used the human KULi003-A iPSC line (BioSamples Cat#SAMEA110177409); iCas9-FL-BCL were used for the inducible system was obtained from Banco Nacional de Líneas Celulares (BNLC).

HepG2 cell line The HepG2 cell line was purchased from Sigma (Cat#8511430).

Staggerer mice All animal experiments were approved by the Ethics Committee of Animal Experimentation of the University of Barcelona and were conducted in accordance with the National Institute of Health Guide for the Care and Use of Laboratory Animals. For the fibrogenic experiments in staggerer mice (sg/sg), mice homozygous for the staggerer spontaneous mutation, both genders of between 8-10 weeks of age were used. Staggerer mice were obtained from the laboratory of Benédicte Antoine.

Specific Knockout (KO) mice for Rora in HSCs All animal experiments were approved by the Ethics Committee of Animal Experimentation of the University of Barcelona and were conducted in accordance with the National Institute of Health Guide for the Care and Use of Laboratory Animals. To investigate the effects of RORA knockout specifically in HSCs within the context of liver fibrosis, a new animal strain was created. This was achieved by crossing RORA floxed (fl/fl)[28] mice with Lrat-Cre[29]. The presence of the floxed allele and the Cre transgene in offspring was confirmed by genotyping. Ten $Rora^{fl/wt}$ mice, including Cre^- and Cre^+ were used to stablish a CCl_4 model of 4 weeks. Mice were injected I.P. with 0.5 mL/kg of CCl_4 (diluted in corn oil) twice a week.

Wild-type (WT) mice All animal experiments were approved by the Ethics Committee of Animal Experimentation of the University of Barcelona and were conducted in accordance with the National Institute of Health Guide for the Care and Use of Laboratory Animals. For

the fibrogenic experiments, C57BL/6 J female and male mice of 8-10 weeks of age were used.

Human samples Liver biopsies from patients diagnosed with liver diseases or controls from liver resections of metastic tumors who were admitted to the Liver Unit at the Hospital Clinic of Barcelona were utilized for this study (HCB/2013/8175). Informed consent was obtained from the patients.

iPSCs differentiation towards diHSCs

iPSCs KULi003-A, clone 5, clone 8 and clone 13 J of RORA$^{+/}$ iPSCs were differentiated following the protocol described previously[19–21]. Results from only clone are shown in the main figures and the other two clones are included in the supplementary material. Briefly, diHSCs differentiation started when iPSCs achieved 70% confluence. From day 0 to day 4, cells were cultured in liver differentiation media (LDM) supplemented with BM4 (20 ng/ml, R&D, Cat#314-BP-010). From day 4 to day 6, cells were treated with BMP4 (20 ng/ml), FGF1(20 ng/ml, R&D, Cat#232-FA-025) and FGF3 (20 ng/ml, R&D, Cat#1206-F3-025). From day 6 to day 8, cells were stimulated with FGF1 (20 ng/ml), FGF3 (20 ng/ml), retinol (5µM, Sigma Aldrich, Cat#R7632-100MG) and palmitic acid (100µM, Sigma Aldrich, Cat#P0500). Finally, from day 8 to day 12, cells were cultured in LDM supplemented with retinol and palmitic acid. Recombinant proteins used for the in vitro assays are referenced in Supplementary table 1.

Generation of heterozygote KO iPSC for RORA gene

Heterozygous RORA-knockout (KO) iPSCs (RORA$^{+/}$) were obtained using the same mutation presented in staggerer mice[37]. The sgRNA "5'-ATCTGTGGAGACAAATCATCAGG-3'" (IDT) was designed by the CRISPR tool (https://bioinfogp.cnb.csic.es/tools/breakingcas). Rock inhibitor at 10µM (Y-27632, BD Bioscience, Cat# 562822) was added to the iPSCs 3 h (h) before nucleofection. 100 pmol Alt-R™ S.p. HiFi Cas9 Nuclease V3 (IDT) was incubated with 120 pmol Alt-R® CRISPR-Cas9 sgRNA (IDT) at 25 °C for 10 min (min). 200,000 cells were dissociated with Accutase (Gibco, Cat#A1110501), washed twice with PBS without Ca and Mg and resuspended with 20µl of P3/S1 Buffer. RNP complex was added to the cells prior to nucleofection in a 20ul cuvette. Cells were nucleofected with the 4-D Nucleofector System (Lonza, Cat#AAF-1003X) using the CA-137 program. Nucleofected cells were cultured in a 12-well plate, with mTSR1 and 10uM of Y- 27632. After 72 h of recovery, 1000 cells were seeded at a single-cell level in a 100 mm plate to generate single-cell colony. Genotyping was performed by PCR and Sanger sequencing from single-cell colonies to analyze the genotype. Two rounds of single-cell cloning were performed to ensure a single-cell clone. For the experiments concerning the constitutive mutation, we used as controls RORA iPSCs wild-type (WT) obtained after the nucleofection process.

Generation of an inducible KO for RORA in iPSCs-based system

To establish an inducible RORA knockout, the same sgRNAs were incorporated into a lentiviral vector. Virus production was achieved by co-transfecting HEK293T cells with the gRORA plasmid and packaging plasmids (psPAX2) using PEI. After incubating for 24 h and changing the media, the viral supernatant was harvested, concentrated via ultracentrifugation, and stored at -80 °C. Induced pluripotent stem cells (iPSCs) (iCas9-FL-BCL)[38] were obtained from the BNCL (Banco Nacional de Lineas Celulares del ISCII) and infected with the lentivirus and selected with hygromycin for one week to ensure stable integration. To activate the knockout, the iCas9-FL-BCL cell line was treated with doxycycline (1 µg/mL), which induced the expression of Cas9.

Chemical modulation of RORA signalling

On day 2 of the differentiation protocol, the synthetic agonist (SR1078, Merck, Cat#557352) or antagonist (SR1001, MCE, Cat#HY-13421) of RORA and RORG was added to the cells at 0.1 mM or 85 nM, respectively. Treatment refresh was performed every two days. Samples were collected at day 12 for further analysis. For the modulation of RORA after passage, differentiated cells at day 12 were passaged as explained previously[20]. Once cells achieved 70% confluence, SR1001 (85 nM) and SR1078 (3 mM) were added for 24 h. Samples were collected for further analysis. Recombinant proteins used for the in vitro assays are referenced in Supplementary Table 1.

Fibrogenic in vitro assay

diHSCs were passaged and treated with TGFβ (Prepotech, Cat#AF-100-21C) at 5 ng/mL for 24 h or 7 days as explained elsewhere[20]. During the last 24 h, SR1078 (3 mM) was added to the cell culture and samples were collected fur further analysis. Recombinant proteins used for the in vitro assays are referenced in Supplementary Table 1.

Co-culture 3D assay

Liver spheroids were generated using diHSCs and HepG2 in a 1:2 ratio. 3000 cells were seeded in a non-adherent U-Shape bottom 96-well plate in DMEM Glutamax, 10% FBS and 1% P/S. Plates were centrifuge at 200 g for 2 min. and placed on the incubator. After 3 days, a half medium change was performed, and experiments started after 5 days of culture. Then, liver spheroids were treated with SR1078 at 3 mM for 24 h; 10 ng/mL for TGFβ during 48 h. During the last 24 h, liver spheroids were also treated with SR1078 3 mM. Samples were collected for further analysis.

In vitro studies with rat neonatal cardiomyocytes (NCMs) and fibroblasts (NCFs)

Rat NCMs were obtained from the ventricles of 1- to 3-day-old Sprague-Dawley rats. Briefly, hearts were digested with a collagenase solution (Collagenase Type I; Life Technologies, Cat# 17100017) and differential plating was performed. NCMs were plated at a density of 0.5 × 106 cells/well on 6-well culture plates and grown for 24 h. NCMs were treated with phenylephrine PE (10 µmol/L; Sigma, Cat#P1240000), as a pathological hypertrophic growth factor for 24 h. Rat neonatal cardiac fibroblasts (NCFs) were isolated from the ventricles of 1- to 2-day-old Sprague-Dawley rats. Passage 1 and 3 cells were plated at a density of 0.3 × 105 cells/cm2 on culture dishes and grown for 24 h.

Sample preparation for proteome analysis

Day 0, day 2, day 4, day 6, day 8, day 10, day 12 and pHSCs were washed once with DPBS -/- and 500 mL of buffer lysis was added to the culture (7 M urea, 2 M thiourea and CHAPS 4%) following the filter aided FASP protocol described elsewhere 22 with minor modifications. Trypsin was added at a trypsin:protein ratio of 1:50, and the mixture was incubated overnight at 37°C, dried out in a RVC2 25 speedvac concentrator (Christ), and resuspended in 0.1% formic acid. Peptides were desalted and resuspended in 0.1% FA using C18 stage tips (Millipore).

Mass spectrometry analysis

Samples were analyzed in a hybrid trapped ion mobility spectrometry −quadrupole time of flight mass spectrometer (timsTOF Pro with PASEF, Bruker Daltonics) coupled online to a nanoElute liquid chromatograph (Bruker). The sample (200 ng) was directly loaded in a 15 cm Bruker nanoelute FIFTEEN C18 analytical column (Bruker) and resolved at 400 nl/min with a 30 min gradient. The column was heated to 50°C using an oven. Protein identification and quantification was carried out with MaxQuant software using default settings. Searches were performed against a database consisting of human protein entries (Uniprot/Swissprot), with precursor and fragment tolerances of 20ppm and 0.05 Da. Only proteins identified with at least two peptides at FDR < 1% were considered for further analysis. Data (LFQ intensities) was loaded onto a Perseus platform 25 and further processed (log2 transformation, imputation). Protein abundances were normalized against the day 0 for each individual.

RNA extraction, cDNA synthesis, qRT-PCR analysis and Bulk RNA sequencing

RNA from cells was obtained using the Quick RNA-Microprep Kit (Zymo, Cat#R1050), following the manufacturer's instructions. For 3D cultures, total RNA from 6 pooled spheroids were extracted using the same kit. Total RNA was extracted from mouse whole liver tissue using Trizol (Life Technologies, Carlsbad, CA, Cat#15596026). The total RNA extracted underwent quality control by Bioanalyzer 2100 (Agilent Technologies, Santa Clara, CA). RNA concentrations were measured using the Nanodrop 1000 (ThermoFisher). cDNA synthesis was performed with the MultiScrib (Applied biosystems, Cat#4368813) followed by a quantitative reverse transcription polymerase chain reaction (qRT-PCR) on an ABI 7900HT cycler (Applied Biosystems) and SYBR green master mix (Life Technologies, Cat#11733046). Gene expression was normalized to *GAPDH* for in vitro systems and *Actb* for in vivo experiments. Expression values were calculated based on the ΔΔCt method. Primers used for gene expression analysis are referenced in Supplementary Table 2. For bulk-RNA sequencing, the quality of RNA was evaluated using Agilent RNA 6000 Nano Chips (Agilent Technologies, Santa Clara, CA, USA). Sequencing libraries were prepared following the TruSeq Stranded mRNA Sample Preparation with the corresponding kit starting from 125 ng of total RNA per sample. Sequencing of the mRNA libraries was performed in a HiSeq2500 (Illumina Inc, San Diego, CA, USA) to obtain at least 30 million 51nt-single-end reads per sample. GO biological processes term enrichemnet, KEGG pathway, Reactome and gene set enrichment analysis were performed using DAVID[39], and GSEA database[40].

Lipidomics

The lipidomics assay was conducted in collaboration with Olobion. In brief, cells were harvested using trypsin and subsequently washed with PBS to eliminate residual media and contaminants. We added 275 μL of methanol directly to the cells along with a ball for homogenization, which was carried out for one minute. Following this, 1 mL of MTBE was incorporated into the mixture, which was then shaken and centrifuged. For lipidomic profiling, we collected 100 μL of the upper organic phase, evaporated it, and resuspended the residue in 100 μL of methanol containing an internal standard. This mixture was shaken, centrifuged, and prepared for LC-MS analysis. The lipids were separated using an ACQUITY UPLC BEH C18 column maintained at 65 °C and analyzed on a ZenoTOF 7600 system (SCIEX). A sample volume of 4 μL was injected in both ESI positive and negative modes, and the lipidomics data were processed using oloMAP 2.0.

Intracellular glucose level testing

Intracellular glucose levels from day 4 differentiated cells and diHSCs passaged cells were assessed using the Glucose-Glo™ Assay, following manufacturer instructions (Promega, Cat#TM494). Briefly, the assay was applied to cells in a 96-well plate. Before beginning the assay, the medium was removed, and the cells were washed with 100 μl of DPBS. To initiate glucose uptake, 50 μl of 2DG in DPBS were used. The uptake reaction was stopped, and the samples were processed following the manufacturer's instructions. Commercial kits used within this manuscript have been collected in Supplementary Table 3.

XF24 extracellular flux

The oxygen consumption ratio (OCR) was determined using the Seahorse XF Cell Mito Stress Test (Agilent, Santa Clara, CA, US). Briefly, iPSC-RORA $^{+/-}$ and their WT counterparts, treated and untreated with the RORA agonist SR1078 at 0.1 mM at day 4 of the differentiation, were sequentially treated with 1 μM oligomycin; 2 μM carbonyl cyanide m-chlorophenyl hydrazone (CCCP); and a 1 μM mixture including rotenone and antimycin A according to manufacturer's instructions. Seahorse XFe Wave Software (Agilent) was applied to analyze the data. Similarly, cells after passage were treated with RORA agonist and/or TGFb for 24 h. Finally, the cell mass was normalized quantified total protein using the BCA protein assay kit (ThermoFisher, Cat# 23225). Commercial kits used within this manuscript have been collected in Supplementary Table 3.

Immunofluorescence and immunohistochemistry

Cells were fixed using 4% Neutral Buffered Formalin for 15 min and washed with PBS for three times before permeabilization at room temperature during 30 min. with 0.2% Triton X-100 in PBS. Afterwards, the cells were blocked with 3% of donkey serum at room temperature. Cells were incubated overnight at 4 °C with primary antibodies in DAKO REALTM Anti-body diluent (Agilent, Cat#S2022). Secondary antibodies (1:500 dilution) were incubated for 30 min. To ensure nuclear staining, samples were mounted with Mounting Medium with 4',6-diamidino-2-phenylindole (DAPI) (Vector Laboratories, Cat# H-1200-10). Antibodies used within this manuscript have been collected in Supplementary Table 4.

RORA immunofluorescence in human tissue

Human liver sections were included in OCT and maintained at -80 °C. Slides were fixed at 4% PFA for 2 min. They were then washed in PBS for a few seconds and blocked in 100 μL 5% BSA in PBS + 0,3% TritonX100 per tissue section during 1 h. Tissue sections were incubated overnight with primary antibodies (RORA 1:50, Abcam, Cat#ab70061) in 5%BSA/PBS/Triton at 4 °C in a dark moist chamber. Then, the sections were incubated 1 h with secondary antibodies in 5%BSA/PBS/Triton at room temperature (RT) in a dark moist chamber. Tissue sections were mounted using the Vectashield Mounting medium for fluorescence with DAPI.

In vivo test in carbon tetrachloride-induced liver fibrosis model in homozygous staggerer mice

To test the physiological role of RORA upon liver fibrosis in vivo, we established a carbon tetrachloride (CCl_4) model based on intraperitoneal (I.P.) injection of 0,5 ml/kg of CCl_4 diluted in corn oil. Mice were injected two days a week during four 4 weeks. Blood and liver tissues were collected for further analysis.

Generation of RORA Knockout (KO) HSC-specific animals

To examine the impact of RORA KO specifically in HSCs in the context of liver fibrosis, we developed a new animal model. This was accomplished by crossing RORA floxed (fl/fl) mice with Lrat-Cre mice. The presence of the floxed allele and the Cre transgene in the offspring was confirmed through genotyping. $n = 5$ Lrat-Cre^{+} Rora$^{fl/-}$ and $n = 5$ Lrat-Cre^{-} Rora$^{fl/-}$ mice were injected i.p. with 0.5 mL/kg of CCl_4 (0.5 mL/kg of CCl_4 diluted in corn oil) twice a week for four weeks. Animals were sacrificed 24 h after the last CCl_4 injection and blood, and liver tissues were collected and analyzed.

In vivo test of RORA as an antifibrogenic target in fibrogenic models

For the liver fibrosis model, 14 C57BL/6 J mice were injected twice a week with CCl4 0,5 ml/kg (25% corn oil) during 4 weeks. During the last 2 weeks, mice were divided into two groups: 1) $n = 7$ mice were injected ip with SR1078 (10 mg/kg) twice a week; 2) $n = 7$ mice were injected ip with vehicle DMSO at the same concentration. SR1078 was diluted in 5% DMSO to a final concentration of 2 mg/ml. For the heart fibrotic model, $n = 10$ C57BL/6 J mice were administered isoproterenol (Sigma Aldrich, Cat#SLC62971) by continuous infusion of 60 mg/kg/day using minipumps (Model 1007D, Alzet). After 24 h, animals were divided into two groups: 1) $n = 5$ treated with SR1078 (10 mg/kg) every 48 h IP and 2) $n = 5$ injected IP with the vehicle during 1. Animals were sacrificed after one week. For the kidney fibrotic model, $n = 19$ C57BL/6 J mice underwent ligation of the left ureter and starting 3 days after surgery, the mice were divided into two groups: 1) $n = 10$ treated with SR1078 (10 mg/kg) from day 3 after surgery until day 15.; 2) $n = 9$ treated with

vehicle from day 3 after surgery for 15 Blood and liver, heart and kidney tissues were collected for further analysis.

Collagen tissue determination

The amount of collagen in liver tissues was determined by measuring the content of hydroxyproline using a Hydroxyproline assay kit (Abcam, Cat#MAK008-1KT) as described by the manufacturer. Absorbance was measured at 540 nm using a FLUOstar OPTIMA FL reader (BMG LABTECH).

Biochemical determination by Echevarne laboratories (Barcelona, Spain)

Serum from mice included in the experimental studies was collected and analyzed for alanine transaminase (ALT), aspartate transaminase (AST), phosphatase alkaline (AP) and lactate dehydrogenase (LDH) values.

Statistical analysis

GraphPad Prism v8.0 was used for the statistical analyses. The D'Agostino-Pearson omnibus normality test, Anderson-Darling test and Shapiro-Wilk normality test were performed to assess data distribution. For statistical analysis of parametric data, the two-tailed unpaired Student's t test was used for groups of two; one-way ANOVA followed by Sidak multiple comparison posthoc tests were used for comparison of more than two groups. For non-parametric data, the Mann-Whitney U test was used for groups of two while the Kruskal-Wallis test followed by the Dunn multiple comparison posthoc test was used for comparison of more than two groups.

Reporting summary

Further information on research design is available in the Nature Portfolio Reporting Summary linked to this article.

Data availability

The proteomic data generated in this study have been deposited in ProteomeXchange Consortium via the PRIDE partner repository under accession code PXD058290. The transcriptomic data generated in this study have been deposited in Gene Expression Omnibus (GEO) database under accession code GSE282539. The transcriptomic data of primary HSCs used in this study are available in the GEO database under accession code GSE90525 and GSE67664. Source data are provided with this paper.

References

1. Weterings, S. D. C., van Oostrom, M. J. & Sonnen, K. F. Building bridges between fields: bringing together development and homeostasis. *Development* **148**, dev193268 (2021).
2. Asahina, K. et al. Mesenchymal origin of hepatic stellate cells, submesothelial cells, and perivascular mesenchymal cells during mouse liver development. *Hepatology* **49**, 998–1011 (2009).
3. Asahina, K., Zhou, B., Pu, W. T. & Tsukamoto, H. Septum transversum-derived mesothelium gives rise to hepatic stellate cells and perivascular mesenchymal cells in developing mouse liver. *Hepatology* **53**, 983–995 (2011).
4. Zhao, X., Kwan, J. Y., Yip, K., Liu, P. P. & Liu, F.-F. Targeting metabolic dysregulation for fibrosis therapy. *Nat. Rev. Drug Discov.* **19**, 57–75 (2019).
5. Taylor, R. S. et al. Association between fibrosis stage and outcomes of patients with nonalcoholic fatty liver disease: a systematic review and meta-analysis. *Gastroenterology* **158**, 1611–1625.e12 (2020).
6. Higashi, T., Friedman, S. L. & Hoshida, Y. Hepatic stellate cells as key target in liver fibrosis. *Adv. Drug Deliv. Rev.* (2017).
7. Friedman, S. L. Evolving challenges in hepatic fibrosis. *Nat. Rev. Gastroenterol. Hepatol.* **7**, 425–436 (2010).
8. Hernandez-Gea, V. & Friedman, S. L. Pathogenesis of liver fibrosis. *Annu. Rev. Pathol.* **6**, 425–456 (2011).
9. Chen, Y. et al. Hedgehog controls hepatic stellate cell fate by regulating metabolism. *Gastroenterology* **142**, 938–946 (2012).
10. Du, K. et al. Hedgehog-YAP signaling pathway regulates glutaminolysis to control activation of hepatic stellate cells. *Gastroenterology* **154**, 1526–1538 (2018).
11. Bates, J. et al. Acetyl-CoA carboxylase inhibition disrupts metabolic reprogramming during hepatic stellate cell activation. *J. Hepatol.* **73**, 896–905 (2020).
12. Wandzioch, E., Kolterud, A., Jacobsson, M., Friedman, S. L. & Carlsson, L. Lhx2/mice develop liver fibrosis. *Dev. Biol.* **270**, 124–133 (2004).
13. Nakano, Y. et al. A deactivation factor of fibrogenic hepatic stellate cells induces regression of liver fibrosis in mice. *Hepatology* **71**, 1437–1452 (2020).
14. Arroyo, N. et al. GATA4 induces liver fibrosis regression by deactivating hepatic stellate cells. *J. Clin. Invest.* **6**, e150059 (2021).
15. Jarvis, C. I. et al. Age-related phenotypes in the staggerer mouse expand the RORα nuclear receptor's role beyond the cerebellum. *Mol. Cell Endocrinol.* **186**, 1–5 (2002).
16. Boukhtouche, F., Mariani, J. & Tedgui, A. The 'CholesteROR' protective pathway in the vascular system. *Arterioscler. Thromb. Vasc. Biol.* **24**, 637–643 (2004).
17. Shajari, S. et al. Melatonin suppresses activation of hepatic stellate cells through RORα-mediated inhibition of 5-lipoxygenase. *J. Pineal Res.* **59**, 391–404 (2015).
18. Choi, H. et al. An RORα agonist, ODH-08, inhibits fibrogenic activation of hepatic stellate cells via suppression of SMAD3. *Life Sci.* **340**, 122443 (2024).
19. Coll, M. et al. Generation of hepatic stellate cells from human pluripotent stem cells enables in vitro modeling of liver fibrosis. *Cell Stem Cell* **22**, 19–32 (2018).
20. Vallverdú, J. et al. Directed differentiation of human induced pluripotent stem cells to hepatic stellate cells. *Nat. Protoc.* **16**, 2542–2563 (2021).
21. de la Torre, R. A. M. G. & Sancho-Bru, P. Differentiation of hepatic stellate cells from pluripotent stem cells. *Methods Mol. Biol.* **2669**, 33–42 (2023).
22. Ölander, M., Wiśniewski, J. R. & Artursson, P. Cell-type-resolved proteomic analysis of the human liver. *Liver Int.* **40**, 1770–1780 (2020).
23. Zhang, D. Y. et al. A hepatic stellate cell gene expression signature associated with outcomes in hepatitis C cirrhosis and hepatocellular carcinoma after curative resection. *Gut* **65**, 1754–1764 (2016).
24. Zhang, Y., Luo, X.-Y., Wu, D.-H. & Xu, Y. ROR nuclear receptors: structures, related diseases, and drug discovery. *Nat. Rev. Drug Discov.* **36**, 71–87 (2014).
25. Khacho, M. et al. Energy metabolism regulates stem cell pluripotency. *Front. Cell Dev. Biol.* **8**, 87 (2020).
26. Chai, C. et al. Agonist of RORA attenuates nonalcoholic fatty liver progression in mice via up-regulation of microRNA 122. *Gastroenterology* **159**, 999–1014.e9 (2020).
27. Molenaar, M. R., van der Molen, Haaker, M. Vaandrager, A. B., Houweling, M. & Helmes, J. B. Lipidomic profiling of rat hepatic stellate cells during activation reveals a two-stage process accompanied by increased levels of lysosomal lipids. *J. Biol. Chem.* **299**, 103042 (2023).
28. Molinaro, A. et al. Liver-specific RORα deletion does not affect the metabolic susceptibility to western-style diet feeding. *Mol. Metab.* **23**, 82–87 (2019).
29. Mederacke, I. et al. Fate tracing reveals hepatic stellate cells as dominant contributors to liver fibrosis independent of its aetiology. *Nat. Commun.* **4**, 3823 (2013).
30. Graupera, I. et al. Molecular characterization of chronic liver disease dynamics: from liver fibrosis to acute-on-chronic liver failure. *JHEP Rep.* **4**, 100482 (2022).

31. Wesley, B. T. et al. Single-cell atlas of human liver development reveals pathways directing hepatic cell fates. *Nat. Cell Biol.* **24**, 1487–1498 (2022).
32. Yang, W. et al. Single-cell transcriptomic analysis reveals a hepatic stellate cell–activation roadmap and myofibroblast origin during liver fibrosis in mice. *Hepatology* **74**, 2774–2790 (2021).
33. Zhao, M. et al. Targeting fibrosis: mechanisms and clinical trials. *Nat. Rev. Gastroenterol. Hepatol.* **7**, 206 (2022).
34. Cliff, T. S. et al. MYC controls human pluripotent stem cell fate decisions through regulation of metabolic flux. *Cell Stem Cell* **21**, 502–516 (2017).
35. Trivedi, P., Wang, S. & Friedman, S. L. The power of plasticity—metabolic regulation of hepatic stellate cells. *Cell Metab.* **33**, 242–257 (2021).
36. Hernández-Gea, V. et al. Autophagy releases lipid that promotes fibrogenesis by activated hepatic stellate cells in mice and in human tissues. *Gastroenterology* **142**, 938–946 (2012).
37. Castaño, J., Romero-Moya, D., Richaud-Patin, Y. & Giorgetti, A. Generation of two heterozygous GATA2 CRISPR/Cas9-edited iPSC lines, R398W and R396Q, for modeling GATA2 deficiency. *Stem Cell Res.* **55**, 102445 (2021).
38. Castaño, J. et al. Generation and characterization of a human iPSC cell line expressing inducible Cas9 in the "safe harbor" AAVS1 locus. *Stem Cell Res.* **21**, 137 (2017).
39. Huang, D. W., Sherman, B. T. & Lempicki, R. A. Systematic and integrative analysis of large gene lists using DAVID bioinformatics resources. *Nat. Protoc.* **8**, 211–227 (2008).
40. Subramanian, A. et al. Gene set enrichment analysis: A knowledge-based approach for interpreting genome-wide expression profiles. *Proc. Natl. Acad. Sci. Usa.* **102**, 15545–15550 (2005).

Acknowledgements

P.S-B. is supported *by Instituto de Salud Carlos III (ISCIII)* "PI20/00765", PI23/00724, "FORT23/00002", "DTS22/00032", AGAUR, "2021 PROD 00035", 23-0356; Dissecting the role of the 14q32 region in hepatoblastoma "Hblast14" Worldwide Cancer Research; PRYCO223102ARME; Scientific Foundation of the Spanish Association Against Cancer (AECC); Q6922, (B-ORG) Plan Complementario de Biotecnología aplicada a la Salud del Plan de Recuperación, Transformación y Resiliencia. Ministerio de Ciencia e Innovación and co-founded the European research and innovation program Horizon HORIZON-HLTH–2022-STAYHLTH-02 under agreement no. 101095679. R.A M-G is funded by *Instituto de Salud Carlos III* "FI18/00215", S.A. received a grant from the *Ministerio de Educación, Cultura y Deporte* "FPU17/04992", C.M is funded by *Centro de Investigación en Red Enfermedades Hepáticas y Digestivas (CIBERehd)*. A.G. is supported by Competitiveness (MINECO PID2020-15591RB-100), La Marató de TV3 (202001-32) and *CERCA Programme/ Generalitat de Catalunya* for institutional support. J.P. is supported by *La Marató de TV3* (202001-32). D.R-M. is supported by *Deutsche José Carreras Leukämie-Stiftung* (DJCLS 13 R/2022). A.M. was funded by MCIN/AEI/10.13039/501100011033/FEDER, UE through the project grants PID2021-123652OB-I00 and RTI2018-097475-A-100; by MCIN/AEI/10.13039/501100011033 and El FSE invest in your future through the contract RYC 2016-19731; by Pfizer grant #77131383; P.R.B. was funded by Ministerio de Universidades fellowships FPU19/05357; M.F.F. was funded by FPU20/01367. M.V.-R. is supported by Proyecto PID2020-119486RB-100 (funded by MCIN/ AEI/ 10.13039/501100011033), Proyecto LABAECC2024 (funded by Asociación Española Contra el Cáncer, AECC), HORIZON-TMA-MSCA-Doctoral Networks 2021 (101073094), and Redes de Investigación 2022 (RED2022-134485-T). This study was funded by Instituto de Salud Carlos III through the Biobanks and Biomodels Platform and co-funded by the European Union (PTC20/00013, PT20/00130, PT23/00009 and PTC23/00002 to N.M.) and by Instituto de Salud Carlos III and European Union—Next Generation EU, Plan de Recuperación Transformación y Resiliencia (TERAV/ISCIII RD21/0017/0018) to N.M; M.C. was funded by Ramon y Cajal programme from the Ministerio de Ciencia e Innovación RYC2019-026662-I. S.A. is funded by la Caixa Foundation "100010434" and the European Union's Horizon 2020 under the Marie Skłodowska-Curie "847648", PID2021-124694OA-I00, MCIN/AEI/ 10.13039/501100011033 and FEDER Una manera de hacer Europa, The European Union grant agreement 101077312*. Ramon y Cajal program RYC2022-036321-I. (* Views and opinions expressed are, however, those of the author(s) only and do not necessarily reflect those of the European Union. Neither the European Union nor the granting authority can be held responsible for them").

Author contributions

R.A.M.G.T. conceived the study, designed and performed the experiments, interpreted the results and wrote the manuscript. J.V., Z.X., S.A., R.F-L., L.Z., M.M-G., B.A-B., P.R-B., M.F-F., A.N-G., A.B.-R., P.S-F., J.P., D.R-M., P.A.G, C.M.S., L.S.V., P.C.V., C.I.C.C., D.M-R., D.E., B.S., B.A., M.A., J.J.L., M.L.M-C., A.G., F.E, performed experiments. M.A. and F.E. performed the proteomic analysis. J.J.L. performed computational analysis. A.M., M. Y. M., performed the SNPs analysis. N.M., D.E., B.S., B.A., M.M-C., A.G., A.P., A.Z., M.V.-R., A.W., I.G., M.C., provided insights. S.A. and P.S-B., conceived the study, interpreted the results, supervised the experiments, and wrote the manuscript.

Competing interests

M.C. and P.S-B. have a patent (EP2016/079464) regarding the hepatic stellate cell differentiation. The remaining authors declare no competing interests.

Additional information

Supplementary information The online version contains supplementary material available at https://doi.org/10.1038/s41467-025-56024-4.

Correspondence and requests for materials should be addressed to Silvia Affo or Pau Sancho-Bru.

Peer review information *Nature Communications* thanks Scott Friedman, Hans Clevers and the other, anonymous, reviewer(s) for their contribution to the peer review of this work. A peer review file is available.

[1]Institut d'Investigacions Biomèdiques August Pi i Sunyer (IDIBAPS), Barcelona, Spain. [2]University of Barcelona, Barcelona, Spain. [3]Centro de Investigación Biomédica en Red de Enfermedades Hepáticas y Digestivas (CIBERehd), Barcelona, Spain. [4]Department of Experimental Pathology, Institute of Biomedical Research of Barcelona, Spanish National Research Council (IIBB-CSIC), Barcelona, Spain. [5]Departament de Bioquímica i Biomedicina Molecular, Facultat de Biologia, Institut de Biomedicina de la Universitat de Barcelona, Universitat de Barcelona, Barcelona, Spain. [6]CIBER Fisitopatologia de la Obesidad y Nutrición, Instituto de Salud Carlos III, Barcelona, Spain. [7]Institute for Research in Biomedicine (IRB Barcelona), The Barcelona Institute of Science and Technology, Barcelona, Spain. [8]Regenerative Medicine Program, Institut d'Investigació Biomèdica de Bellvitge (IDIBELL), Barcelona, Spain. [9]Gene Regulatory Control in Disease Laboratory, Center for Research in Molecular Medicine and Chronic Diseases (CIMUS), Instituto de Investigación Sanitaria de Santiago de Compostela (IDIS), University of Santiago de Compostela, Santiago de Compostela, Spain. [10]Molecular Psychiatry Laboratory, Division of Psychiatry, University College London, London WC1E 6DE, UK. [11]UCL Institute for Liver & Digestive Health, Division of Medicine, Royal Free Campus, University College London, London NW3 2PF, UK. [12]Pluripotency for Organ Regeneration, Institute for Bioengineering of Catalonia (IBEC), Barcelona Institute of Science and Technology (BIST), Carrer de Baldiri i Reixac, 15-21, Barcelona, Spain. [13]Catalan Institute for Research and Advanced Studies (ICREA), Passeig de Lluís Companys 23, Barcelona, Spain. [14]Univ. Lille, Inserm, CHU Lille, Institut Pasteur de Lille, U1011-EGID, 59000 Lille, France. [15]Sorbonne Université, Inserm, Centre de Recherche Saint-Antoine, CRSA, F-75012 Paris, France. [16]Proteomics Platform, CIC BioGUNE, Basque Research and Technology Alliance (BRTA), Bizkaia Science and Technology Park, Derio, Spain. [17]Liver Disease Lab, Center for Cooperative Research in Biosciences (CIC bioGUNE), Basque Research and Technology Alliance (BRTA), Bizkaia Technology Park, Building 801A, Derio, Spain. [18]Department of Pathology and Experimental Therapeutics, Faculty of Medicine and Health Sciences, Barcelona University, Barcelona, Spain. [19]Department of Biochemistry and Molecular Biology, University of Santiago de Compostela, Plaza do Obradoiro s/n, Santiago de Compostela, Spain. [20]Oportunius Research Professor at CIMUS/USC, Galician Agency of Innovation (GAIN), Xunta de Galicia, Santiago de Compostela, A Coruña, Spain. [21]Centro de Investigación Biomédica en Red de Diabetes y Enfermedades Metabólicas Asociadas (CIBERDEM), Instituto de Salud Carlos III, 28029 Madrid, Spain. [22]Liver Unit, Hospital Clínic, Faculty of Medicine, University of Barcelona, Barcelona, Spain. [23]Medicine Department, Faculty of Medicine, University of Barcelona, Barcelona, Spain. ✉e-mail: saffo@recerca.clinic.cat; psancho@recerca.clinic.cat